Efficient two-stage modal identification for structures with closely spaced modes by Bayesian FFT and joint approximate diagonalization

Dingxuan Xie[1,2], Li Wang [1], Shuo Li[1], Hamed Haddad Khodaparast[2], Michael I Friswell[2], and Zhong-Rong Lu[*,1]

[1]School of Aeronautics and Astronautics, Sun Yat-sen University, Shenzhen Campus, Shenzhen 518107, P.R. China
[2]Faculty of Science and Engineering, Swansea University, Bay Campus, Fabian Way, Swansea, SA1 8EN

Abstract

Modal parameter identification plays a crucial role in structural health monitoring and vibration analysis, as it provides key insights into the dynamic characteristics of structures. While Bayesian statistics effectively address uncertainties in measurement and system identification; however existing methods face challenges with closely spaced modes. A recently developed expectation-maximization (EM) algorithm has shown promise in most scenarios. However, the Bayesian goal function has multiple local extrema, especially for closely spaced mode shapes, and selecting an appropriate initial guess to obtain accurate and fast identification remains a challenge. To circumvent the limitation, an innovative two-stage Bayesian method is proposed with improved efficiency and robustness for modal parameter identification on structures with closely spaced modes. In doing so, the posterior distribution is established via the Bayesian FFT analysis and then, the most probable modal parameters are searched in two sequential stages. In the first stage, the closely spaced mode shapes are found pertaining to a joint approximate diagonalization problem, which can be quickly solved by the Jacobi rotation algorithm, without the need to specify an initial guess. Subsequently in the second stage, the natural frequencies and damping ratios are simply obtained through Newton iteration. The two-stage method decouples the optimization procedure and therefore, can substantially improve the identification efficiency. Numerical simulations and experimental data are analyzed to validate our method, demonstrating its superior efficiency and accuracy modal identification in the presence of closely spaced modes.

Keywords: Operational modal analysis; Bayesian FFT; Closely spaced modes; Joint approximate diagonalization; Two-stage method.

1 Introduction

Operational Modal Analysis (OMA) [1, 2, 3] is a powerful and widely used technique for extracting modal parameters of civil engineering structures [4], mechanical systems [5], and other vibrating systems under ambient or operational conditions. The ultimate goal of OMA is to obtain modal information of structures, including natural frequencies, damping ratios, and mode shapes, without the need for artificial excitation sources.

Early studies in modal testing were developed by Experimental Modal Analysis (EMA) methods [6]. In EMA, the structure is subjected to excitation by one or more quantifiable dynamic forces.

*Correspondence to: Zhong-Rong Lu, Email: lvzhr@mail.sysu.edu.cn

The structure's response to these forces is then recorded, and the modal parameters within the frequency range of interest are derived from these measurements. However, the application of EMA comes with certain limitations. EMA methods face challenges in effectively dealing with large and operational structures. Another issue is that the contribution of the measurable excitation to the total structural response is often minimal. Additionally, it is difficult to control or accurately measure all the sources of excitation that impact the structure. OMA emerges as a response to these limitations and offered a more versatile and cost-effective alternative for modal parameter identification [7]. The main concept behind OMA is to utilize the ambient or naturally occurring excitation sources, such as wind [8], traffic [9], or random vibrations, to analyze the dynamic response of the structure. Various OMA methods have been developed to handle different types of ambient excitation and varying structural characteristics. Early OMA methods, such as peak picking (PP) [10] and random decrement [11], are straightforward in application but only offer approximate estimates of modal parameters. Later, more advanced methods emerged, notably the Frequency Domain Decomposition (FDD) method [12] and the Stochastic Subspace Identification (SSI) [13]. These techniques, known for their good accuracy in estimating modal parameters across a wide range of scenarios, have gained significant attention in the OMA field. In subsequent years, various algorithms [14, 15] have been introduced, aiming not only to identify modal parameters but also to assess the associated uncertainties [16] by means of perturbation. In this respect, Liu et al. [17] proposed an unsupervised self-coding neural network capable of blindly separating and identifying structural modal parameters directly from output-only vibration data. Fevotte et al. [18] introduced Student t-priors for sparse source separation, demonstrating enhanced robustness to ill-conditioned mixing matrices and superior audio quality compared to Gaussian mixture models. More recently, Bayesian methods have gained popularity in various fields [19, 20, 21] due to their proficiency in handling data uncertainties and noise. Bayesian statistics provide a robust framework for parameter estimation, integrating the prior knowledge and information into the estimation process. The foundation of the Bayesian modal identification method in both time and frequency domains was laid by [22, 23]. Initially, these Bayesian methods encountered challenges due to their computational complexity. Moreover, time-domain Bayesian modal identification methods face inherent limitations as they require information from across the entire frequency band [24]. To address these challenges, a Fast Bayesian Fourier Transform (Bayesian FFT) approach [24] was introduced in a well-separated modes situation, for approximating the posterior covariance matrix of modal parameters, validated with synthetic and field data in large-scale systems. Subsequent effort has been focused on formulating uncertainty laws [25, 26]. They provide an in-depth exploration of Bayesian methods in operational modal analysis, particularly focusing on the theory, computation, and practical applications of these methods in the context of structural engineering. Ongoing research continues to focus on the development of the Bayesian approach for OMA [27] which incorporates an Expectation-Maximization (EM) algorithm that allows for an analytical update of modal parameters across multiple setups.

The challenge of accurately identifying closely spaced modes is a significant hurdle in OMA. In response to this challenge, an iterative Bayesian OMA algorithm tailored for multi-mode problems is proposed [28]. This algorithm represents mode shapes in an orthogonal basis along with their associated coordinates, allowing for the updating of the most probable value (MPV) of modal parameters until convergence [29]. Nonetheless, ensuring convergence, particularly in scenarios with three or more modes within a selected frequency band, remains a substantial challenge. To address the convergence issue, a more robust solution, based on the EM algorithm [30], is introduced. This method enhances the efficiency of computing MPVs for multiple modes. Further refinement came with the integration of a parameter-expansion EM (PX-EM) algorithm [31], which substantially accelerates the convergence process and improves the performance of the iterative EM algorithm for modal identification in the presence of closely spaced modes. Recently, a highly efficient Fisher information matrix (FIM)-driven optimization method [32] is developed to significantly reduce computation time and improve convergence robustness compared to existing approaches. Furthermore, building directly upon the

EM formulations, a modified Newton algorithm [33] for Bayesian OMA is introduced. By leveraging Fisher's identity for gradient computation, this method achieves faster processing speeds than the conventional EM algorithm.

These advancements in Bayesian OMA have shown impressive results in the accurate and efficient identification of closely spaced modes across various structural systems, and become increasingly important in the field of vibration analysis and structural health monitoring.

However, choosing an appropriate initial guess for the EM algorithm remains an challenging issue. Since the Bayesian goal function has multiple local extrema and the EM algorithm is inherently a local optimization method, the choice of initial value significantly impacts the identification results. A poor initial value selection can even lead to inaccurate and costly identification.

In this paper, we introduce a novel two-stage Bayesian method to address the accuracy and efficiency issues of existing Bayesian OMA for identifying closely spaced modes. It follows the Bayesian FFT goal function [24], but finds the most probable value in a more efficient and accurate two-stage procedure. In the first stage, optimization of the goal function with respect to the mode shapes is recast into a joint approximate diagonalization (JAD) problem, which is quickly solved by the Jacobi rotation algorithm, without the need to specify an initial guess. This clearly circumvents the challenging issue on the requirement of an appropriate initial guess of the closely spaced mode shapes for the EM algorithm. Subsequently, in the second stage, the modal frequencies and damping ratios are obtained by Newton iteration of the goal function. This two-stage methodology aims to effectively tackle the challenges posed by closely spaced modes in Bayesian FFT-based modal analysis. It offers several key features, which are summarized as follows

- It searches the closely spaced mode shapes in the JAD problem setting by the well-known Jacobi rotation algorithm. There is no need to specify the initial guess, thus circumventing the challenging issue on the requirement of an appropriate initial guess of the closely spaced mode shapes for existing Bayesian OMA.
- It decouples the whole optimization problem into two subsequent stages, substantially improving the identification efficiency.
- In comparison to the competitive EM algorithm [30], it has been shown in later testing examples to give more accurate identification of closely spaced modes, especially when the frequencies are very close. This is attributed to the fact that the resonance peaks of the close modes are coupled so that the selection of the initial frequencies and mode shapes may be unsatisfactory.

The remainder of this paper is organized as follows. Section 2 offers a concise introduction to Bayesian FFT theory, laying the groundwork for subsequent discussions and addressing the challenge of modal identification in the presence of closely spaced modes. In Section 3, a novel two-stage method is developed to search the most probable value, where the mode shapes are identified in the first stage by solving the JAD problem, while the natural frequencies and damping ratios are obtained subsequently in the second stage by Newton iteration. Numerical and experimental examples are studied in Sections 4, 5 and 6 to demonstrate the performance of the proposed method. Final conclusions are summarized in Section 7.

2 Bayesian FFT framework for identifying closely spaced modes

The ambient vibration time history data, denoted as $\hat{\mathbf{y}}_j$ for $j = 1, ..., N$, measured across n channels with N samples per data channel, undergoes a scaled Fast Fourier Transform denoted as $\hat{\mathbf{F}}_k$,

$$\hat{\mathbf{F}}_k = \sqrt{\Delta t/N} \sum_{j=1}^{N} \hat{\mathbf{y}}_j \mathrm{e}^{-2\pi \mathrm{i}(j-1)(k-1)/N} \tag{1}$$

where Δt signifies the time interval between two samples, and $\mathrm{i} = \sqrt{-1}$ is the imaginary unit. The sampling rate must adhere to the Nyquist theorem for accurate signal reconstruction. Herein, $\hat{\mathbf{F}}_k$ corresponds to the Fourier transform at the frequency $f_k = k/(N\Delta t)$. The FFT in Eq. (1) is scaled by the factor $\sqrt{\Delta t/N}$ so that the expectation of $\hat{\mathbf{F}}_k\hat{\mathbf{F}}_k^*$ (where $\hat{\mathbf{F}}_k^*$ denotes conjugate transpose of $\hat{\mathbf{F}}_k$) is equal to the two-sided power spectral density (PSD) matrix of the data process.

In practical modal identification [26], the frequencies f_k in analysis are selected within a relatively compact frequency band with N_f points to cover a single well-separated mode or several closely-spaced modes of interest. Without loss of generality and for simplicity, these frequency points are designated as $f_1, f_2, ..., f_{N_f}$ for later analysis. This selection balances the amount of information for identification and the model errors. It is assumed that the scaled FFT is contaminated by measurement errors, such as data noise. The relationship between the uncontaminated structural response and the contaminated one is expressed as

$$\hat{\mathbf{F}}_k = \mathbf{F}_k + \epsilon_k \tag{2}$$

where $\mathbf{F}_k$ and ϵ_k are theoretical scaled FFT and the prediction error respectively.

Suppose that the selected frequency band is predominantly influenced by m vibration modes. For a well-separated mode, there is $m = 1$, while in the presence of closely spaced modes, $m \geq 2$ generally equal to the number of closely spaced modes. Thus, it is naturally to set $m \leq n$. In this context, we can express $\hat{\mathbf{F}}_k$ as the superposition of the m partial mode shapes $\mathbf{\Phi} = [\phi_1, \phi_2, \dots \phi_m]$

$$\hat{\mathbf{F}}_k = \mathbf{\Phi}\eta_k + \epsilon_k = \mathbf{\Phi}\mathbf{h}_k\mathbf{p}_k + \epsilon_k \tag{3}$$

where $\phi_i \in \mathbb{R}^{n\times 1}$ is the ith mode shape within the frequency band, and is scaled by ℓ^2-norm, i.e., $||\phi_i|| = 1$ with $||\cdot||$ denoting the ℓ^2-norm of a vector. $\eta_k = \mathbf{h}_k\mathbf{p}_k$ is the scaled FFT of the modal response at frequency f_k and $\mathbf{p}_k$ is the scaled FFT of the modal force at frequency f_k. $\mathbf{h}_k = \mathrm{diag}(h_{1k}, h_{2k}, \dots, h_{mk})$ is a diagonal matrix with transfer functions at frequency f_k filled in its diagonal elements. The transfer function, for the ith mode and at frequency f_k, is given by

$$h_{ik} = \frac{(2\pi \mathrm{i} f_k)^{-q}}{1 - \beta_{ik}^2 - \mathrm{i}\,(2\zeta_i\beta_{ik})}, \qquad \text{with } q = \begin{cases} 0, & \text{acceleration data} \\ 1, & \text{velocity data} \\ 2, & \text{displacement data} \end{cases} \tag{4}$$

where $\beta_{ik} = f_i/f_k$ and ζ_i are the frequency ratio and damping ratio, respectively. f_i the natural frequency of the ith mode.

The modal forces are assumed to have a constant PSD matrix $\mathbf{S}$ ($m \times m$ Hermitian) in the frequency band, whose (i, j) entry is $S_{ij} = \mathbb{E}[p_{ik}p_{jk}^*]$ with $\mathbb{E}[\cdot]$ the expectation operator. The prediction errors at different measured DOFs are assumed to have a constant PSD $\mathbf{S}_e = \mathbb{E}[\epsilon_k\epsilon_k^*] = S_e\mathbf{I}$, where $\mathbf{I}$ is the identity matrix. The assumption of statistical independence between modal excitation and prediction error leads to a jointly independent complex Gaussian distribution for $\hat{\mathbf{F}}_k$, with zero mean and covariance matrix

$$\mathbf{E}_k = \mathbb{E}[\mathbf{F}_k\mathbf{F}_k^*] + \mathbb{E}[\epsilon_k\epsilon_k^*] = \mathbf{\Phi}\mathbf{H}_k\mathbf{\Phi}^T + S_e\mathbf{I} \tag{5}$$

where $\mathbf{H}_k = \mathbb{E}[\eta_k\eta_k^*] = \mathbf{h}_k\mathbf{S}\mathbf{h}_k^*$ is the PSD (or covariance) of the modal responses.

The covariance matrix $\mathbf{E}_k$ holds pivotal importance in Bayesian OMA, influencing the likelihood function through the set of modal parameters $\boldsymbol{\theta} = (\mathbf{f}, \zeta, \mathbf{\Phi}, \mathbf{S}, S_e)$ to be identified. The parameters include natural frequencies $\mathbf{f} = [f_1, f_2, \dots, f_m]$ and damping ratios $\zeta = [\zeta_1, \zeta_2, \dots, \zeta_m]$, and serve as a critical tool for accommodating uncertainties and noise in the measured data, directly impacting the accuracy and reliability of the parameter estimation process.

By applying Bayes' Theorem, the posterior of $\boldsymbol{\theta}$ given a number of frequency responses $\{\hat{\mathbf{F}}_k\}_{k=1}^{N_f}$ in the analysis frequency band is expressed as

$$p(\boldsymbol{\theta}|\{\hat{\mathbf{F}}_k\}_{k=1}^{N_f}) = \frac{p(\{\hat{\mathbf{F}}_k\}_{k=1}^{N_f})|\boldsymbol{\theta})p(\boldsymbol{\theta})}{p(\{\hat{\mathbf{F}}_k\}_{k=1}^{N_f})} \tag{6}$$

where the term $p(\{\hat{\mathbf{F}}_k\}_{k=1}^{N_f})$ represents the marginal likelihood, acting as a normalization constant to ensure the integration of the posterior density to one. The likelihood function often exhibits rapid variation compared to the prior, especially with typical data sizes. Assuming, without loss of generality, that $p(\boldsymbol{\theta})$ is non-informative and follows a uniform distribution, the posterior density becomes directly proportional to the complex Gaussian likelihood function

$$p(\boldsymbol{\theta}|\{\hat{\mathbf{F}}_k\}_{k=1}^{N_f}) \propto p(\{\hat{\mathbf{F}}_k\}_{k=1}^{N_f}|\boldsymbol{\theta}) = \prod_{k=1}^{N_f} p(\hat{\mathbf{F}}_k|\boldsymbol{\theta}) = \frac{\pi^{-nN_f}}{\prod_{k=1}^{N_f}|\mathbf{E}_k(\boldsymbol{\theta})|} \mathrm{e}^{-\sum_{k=1}^{N_f}\hat{\mathbf{F}}_k^* \mathbf{E}_k(\boldsymbol{\theta})^{-1}\hat{\mathbf{F}}_k} \tag{7}$$

where $|.|$ denotes the matrix determinant. In general, the negative log-likelihood function (NLLF) is tackled as the goal function for optimization,

$$L(\boldsymbol{\theta}) = -\ln p(\{\hat{\mathbf{F}}_k\}_{k=1}^{N_f}|\boldsymbol{\theta}) = nN_f \ln\pi + \sum_{k=1}^{N_f}\left(\ln|\mathbf{E}_k(\boldsymbol{\theta})| + \hat{\mathbf{F}}_k^* \mathbf{E}_k(\boldsymbol{\theta})^{-1}\hat{\mathbf{F}}_k\right). \tag{8}$$

The posterior distribution demonstrates a unique maximum at the most probable value (MPV), signifying the estimation of modal parameters that best align with the observed data. To approximate the posterior PDF, a second-order Taylor expansion around the MPV establishes a Gaussian approximation

$$p(\boldsymbol{\theta}|\{\hat{\mathbf{F}}_k\}_{k=1}^{N_f}) \approx (2\pi)^{-n_\theta/2}|\hat{\mathbf{C}}|^{-1/2}\mathrm{e}^{-\frac{1}{2}(\boldsymbol{\theta}-\hat{\boldsymbol{\theta}})^T\hat{\mathbf{C}}^{-1}(\boldsymbol{\theta}-\hat{\boldsymbol{\theta}})} \tag{9}$$

where n_θ denotes the number of parameters $\boldsymbol{\theta}$ in the model, $\hat{\boldsymbol{\theta}}$ represents the MPV obtained at the minimal of NLLF (8), and $\hat{\mathbf{C}}$ is the covariance matrix, as the inverse of the Hessian of NLLF at the MPV. In other words, the mean $\hat{\boldsymbol{\theta}}$ and covariance $\hat{\mathbf{C}}$ of posterior Gaussian approximation are computed as,

$$\hat{\boldsymbol{\theta}} = \arg\min_{\boldsymbol{\theta}} L(\boldsymbol{\theta}), \qquad \hat{\mathbf{C}}^{-1} = \frac{\partial^2 L(\boldsymbol{\theta})}{\partial\boldsymbol{\theta}\partial\boldsymbol{\theta}}|_{\boldsymbol{\theta}=\hat{\boldsymbol{\theta}}} \tag{10}$$

where the process to calculate the covariance $\hat{\mathbf{C}}$ (as the inverse Hessian of the NLLF) is elaborated in **Appendix B**, which is the reproduction of the result in Ref. [29]. Both the MPV $\hat{\boldsymbol{\theta}}$ and the covariance matrix $\hat{\mathbf{C}}$ rely on the FFT data $\hat{\mathbf{F}}_k$ and are computable upon data provision.

To get the desired results in Eq.(10), the key ingredient lies in finding $\hat{\boldsymbol{\theta}}$, that corresponds to minimal NLLF. This process can be computationally demanding, particularly for a large number of modal parameters n_θ. To address this issue, efficient algorithms have been proposed in [24] for dealing with well-separated modes. These algorithms offer reliable computation of the MPV and the posterior covariance matrix in most applications, however, may face challenge for closely-spaced modes.

To get an impression on the difficulty when dealing with closely spaced modes, a simple illustrative example is presented. A two-DOF system with closely-spaced modes is considered with frequencies $f_1 = 1\text{Hz}, f_2 = 1.02\text{Hz}$, damping ratios $\zeta_1 = 1\%, \zeta_2 = 1.2\%$, mass-normalized mode shapes $\phi_1 = [1,1]^T, \phi_2 = [-1,1]^T$. The modal excitations $p_i(t)(i=1,2)$ are enforced as stationary Gaussian white noise with PSD $S_{12} = 0, S_{11} = S_{22} = 1$. Synthetic data was generated without considering noise and then, the NLLF $L(\boldsymbol{\theta})$ can be established for different modal parameters $\boldsymbol{\theta}$. Note that for closely spaced mode identification, the frequencies are generally easily and well identified, while the identified mode shapes may not be so satisfactory [34]. Thus, how $L(\boldsymbol{\theta})$ varies with the mode shapes is investigated in detail. To do so, representing the two mode shapes in the following parametric form

$$A = [1,\alpha], B = [1,\beta], \phi_1 = \frac{A}{||A||}^T, \phi_2 = \frac{B}{||B||}^T \tag{11}$$

and fixing exactly other modal parameters, the relation between $L(\boldsymbol{\theta})$ and the mode shape parameters α, β is displayed in Figure 1. Observations from the figure reveal that though the NLLF reaches its

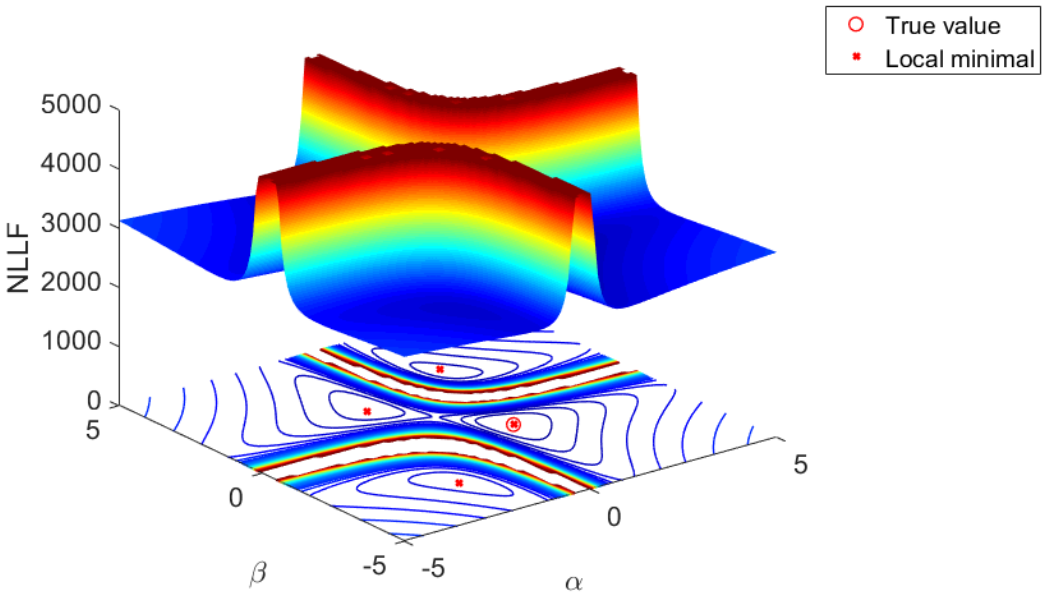

Figure 1: NLLF versus mode shape parameters for a two-DOF system with closely spaced modes

minimum value at the exact mode shape parameters $(\alpha, \beta) = (1, -1)$, the NLLF has multiple local minima. Since the gradient-based algorithm is adopted for optimization, it may converge to incorrect local minima if the initial guess for iteration is improperly chosen and this constitutes one key difficulty in closely-spaced modal identification. Considering this, the process to get the MPV of the NLLF within the Bayesian framework is mainly two-fold,

- *Select a good initial guess of modal parameters.* In previous Bayesian methods [30, 28], the initial guess for mode shapes typically adheres to an ideal derived from within the selected frequency band,

$$\mathbf{D} = \mathrm{Re}\left(\sum_{k=1}^{N_f} \hat{\mathbf{F}}_k \hat{\mathbf{F}}_k^*\right) = \sum_{k=1}^{N_f} (\mathrm{Re}\hat{\mathbf{F}}_k \mathrm{Re}\hat{\mathbf{F}}_k^T + \mathrm{Im}\hat{\mathbf{F}}_k \mathrm{Im}\hat{\mathbf{F}}_k^T) \tag{12}$$

  where Re and Im denote the real and imaginary parts, respectively. The initial frequencies are selected at the peak of the spectrum curve and the initial mode shapes were set as the principal eigenvectors (or singular vectors) of Eq. (12). In fact, this choice is to some extent equivalent to the FDD method [12], which derives the mode shapes from the singular value decomposition of the PSD matrix at the peak frequency. The selected initial mode shapes by the FDD-type method are rather satisfactory for well-separated modes. However, the performance is substantially degraded for closely-spaced modes, because by this way, the modal assurance criterion (MAC) between the identified and exact mode shapes has been shown to be less than 0.90 in some cases [35]. This unsatisfactory result as initial guess may make the convergence towards a undesired local minimal and moreover, less accurate initial guess would generally requires more iterations and hence more computation cost to achieve the convergence. In this work, identifying the mode shapes is reformulated into the JAD problem. The JAD problem can then be tackled by the well-known Jacobi rotation algorithm without the need to specify

the initial guess, circumventing the difficulty in providing a good initial guess for closely-spaced mode shapes. The details are presented in Section 3.1.

It is worth mentioning that selecting the initial guess for natural frequencies and damping is just as important as the initial guess of mode shapes in Bayesian methods. In the identification of closely spaced modes, the coupled peaks of the spectral curves can make the selection of initial natural frequencies challenging because slight perturbation of the close natural frequencies may lead to substantial change of mode shapes. Nevertheless, in this work, the identification of mode shapes and of natural frequencies are decoupled so that the mode shape identification is irrelevant to initial natural frequencies and therefore, the whole process is less sensitive to initial guess of natural frequencies.

- *Design a proper iterative algorithm to reach the minimal.* Unlike the EM algorithm in previous Bayesian methods [30, 28], this work searches the MPV of the NLLF in two sequential and decoupled stages, leading to evident improvement in computation efficiency. How the two-stage method proceeds is specified in Section 3.1.

3 Two-stage method for fast search of the most probable value

In this section, a novel two-stage method is developed to get the MPV of the NLLF (8). In doing so, the parameters $\boldsymbol{\theta}$ are divided into two sets: mode shape related parameters $(\boldsymbol{\Phi}, S_e)$ and natural frequencies/damping ratios related parameters $(\mathbf{f}, \boldsymbol{\zeta}, \mathbf{S})$. Then, the two sets of parameters are optimized in two sequential stages. For later derivation, it is noteworthy that the modal responses are almost mutually uncorrelated so that the PSD of the modal responses $\mathbf{H}_k$ is well approximated by a diagonal matrix [2, 36, 37]. The approximate diagonality of the modal response PSD $\mathbf{H}_k$ plays a key role in the presentation of the proposed method and therefore, is specifically illustrated in **Appendix A**. Thus, from here on, it is directly assumed that $\mathbf{H}_k$ is a diagonal (and thereof, real) matrix and by $\mathbf{H}_k = \mathbb{E}[\eta_k \eta_k^*] = \mathbf{h}_k \mathbf{S} \mathbf{h}_k^*$, only the diagonal part of the force PSD $\mathbf{S}$ will contribute to $\mathbf{H}_k$. Note that this does not mean that non-diagonal parts of $\mathbf{S}$ are 0, but the contribution of non-diagonal parts of $\mathbf{S}$ to $\mathbf{H}_k$ is negligible so that only diagonals S_{ii} arise in $\mathbf{H}_k$ as well as in the NLLF. Considering this, the computation of the covariance in **Appendix B** is also slightly changed in the way that non-diagonal parts $S_{ij}, i \neq j$ is set to 0 and $S_{ij}, i \neq j$ related derivatives are omitted to get a reduced Hessian matrix, that is, $\hat{\mathbf{C}}^{-1} = \frac{\partial^2 L(\boldsymbol{\theta})}{\partial \boldsymbol{\theta} \partial \boldsymbol{\theta}}|_{\boldsymbol{\theta}=\hat{\boldsymbol{\theta}}}$ is obtained with $\boldsymbol{\theta}$ excluding $S_{ij}, i \neq j$.

3.1 Stage 1: Identifying mode shapes by joint approximate diagonalization

Distinct to the conventional JAD applications on PSD matrices or correlation functions [38], this work embeds JAD into the Bayesian FFT likelihood framework. This integration enables two key advances: (i) rigorous formulation of mode shape identification at the MPV of the posterior distribution and (ii) utilization of the celebrated Jacobi rotation algorithm to solve the resulting JAD problem without requiring initial guesses.

To begin with, turn again to the matrix $\mathbf{D}$ in Eq. (12) and the expression in Eq. (3), it is easily obtained under small measurement noise ϵ_k (or high signal to noise ratio) that

$$\mathbf{D} = \mathrm{Re}\left(\sum_{k=1}^{N_f} \hat{\mathbf{F}}_k \hat{\mathbf{F}}_k^*\right) \approx \boldsymbol{\Phi} \mathrm{Re}\left(\sum_{k=1}^{N_f} \eta_k \eta_k^*\right) \boldsymbol{\Phi}^T, \tag{13}$$

indicating that $\mathbf{D}$ is a $n \times n$ matrix with the rank equaling approximately to m $(m \leq n)$. Taking singular value decomposition (SVD) of $\mathbf{D}$, it is easily obtained that

$$\mathbf{D} = \mathbf{U} \boldsymbol{\Sigma} \mathbf{U}^T \approx \mathbf{U}_m \boldsymbol{\Sigma}_m \mathbf{U}_m^T \tag{14}$$

where $\mathbf{\Sigma}_m$ contains the first m singular values and would be substantially larger than the rest $n-m$ singular values. $\mathbf{U} = [\mathbf{U}_m, \mathbf{U}_{m\perp}]$ with $\mathbf{U}_m$ the singular vectors corresponding to $\mathbf{\Sigma}_m$. By Eqs. (13) and (14), $\mathbf{\Phi}$ would span the same vector space as $\mathbf{U}_m$ so that $\mathbf{\Phi}$ is linearly related to $\mathbf{U}_m$ as [29]

$$\mathbf{\Phi} = \mathbf{U}_m \sqrt{\mathbf{\Sigma}_m} \mathbf{R} \tag{15}$$

where $\mathbf{R}$ is a $m \times m$ real and invertible matrix. In this way, obtaining the mode shapes is identical to determining the invertible matrix $\mathbf{R}$. To simplify the process and reduce the mathematical complexity, further derivations of $|\mathbf{E}_k|$ and $\mathbf{E}_k^{-1}$ using the form of mode shapes in Eq. (15) are performed as follows. Initially, substituting Eq. (15) into Eq. (5) yields

$$\mathbf{E}_k = \mathbf{U}_m \sqrt{\mathbf{\Sigma}_m} \mathbf{R} \mathbf{H}_k \mathbf{R}^T \sqrt{\mathbf{\Sigma}_m} \mathbf{U}_m^T + S_e \mathbf{I}_n = \mathbf{U} \begin{bmatrix} \mathbf{E}_k^{'} & 0 \\ 0 & S_e \mathbf{I}_{n-m} \end{bmatrix} \mathbf{U}^T \tag{16}$$

where

$$\mathbf{E}_k^{'} = \sqrt{\mathbf{\Sigma}_m} \mathbf{R} \mathbf{H}_k \mathbf{R}^T \sqrt{\mathbf{\Sigma}_m} + S_e \mathbf{I}_m. \tag{17}$$

With Eq. (16) and the fact that $\mathbf{U}$ is an orthonormal matrix, it is easily deduced that

$$|\mathbf{E}_k| = |\mathbf{U}||\mathbf{E}_k^{'}||S_e \mathbf{I}_{n-m}||\mathbf{U}^T| = S_e^{n-m} |\mathbf{E}_k^{'}| \tag{18}$$

and

$$\mathbf{E}_k^{-1} = \mathbf{U} \begin{bmatrix} \mathbf{E}_k^{'-1} & 0 \\ 0 & S_e^{-1} \mathbf{I}_{n-m} \end{bmatrix} \mathbf{U}^T = \mathbf{U}_m \mathbf{E}_k^{'-1} \mathbf{U}_m^T + S_e^{-1} \mathbf{U}_{m\perp} \mathbf{U}_{m\perp}^T. \tag{19}$$

Now incorporating Eq. (18) and Eq. (19) into Eq. (8) yields

$$L(\boldsymbol{\theta}) = n N_f \ln \pi + (n-m) N_f \ln S_e + \sum_{k=1}^{N_f} \ln |\mathbf{E}_k^{'}| + S_e^{-1} (d - d^{'}) + \sum_{k=1}^{N_f} \hat{\mathbf{F}}_k^* \mathbf{U}_m \mathbf{E}_k^{'-1} \mathbf{U}_m^T \hat{\mathbf{F}}_k \tag{20}$$

where

$$d = \sum_{k=1}^{N_f} \hat{\mathbf{F}}_k^* \hat{\mathbf{F}}_k, \quad d^{'} = \sum_{k=1}^{N_f} \hat{\mathbf{F}}_k^* \mathbf{U}_m \mathbf{U}_m^T \hat{\mathbf{F}}_k \tag{21}$$

so that $d - d^{'} = \sum_{k=1}^{N_f} \hat{\mathbf{F}}_k^* \mathbf{U}_{m\perp} \mathbf{U}_{m\perp}^T \hat{\mathbf{F}}_k \geq 0$ if $n \geq m$. In the following, minimizing the goal function (20) with respect to S_e and $\mathbf{R}$ will be presented:

(a) *Minimization with respect to* S_e

Normally, in case of high signal to noise ratio ($\mathbf{I}_m - S_e \mathbf{E}_k^{'-1} \approx \mathbf{I}_m$), $\mathbf{E}_k^{'}$ in Eq. (17) is dominated by the first term and is insensitive to S_e [29]. That is to say, $\mathbf{E}_k^{'} \approx \sqrt{\mathbf{\Sigma}_m} \mathbf{R} \mathbf{H}_k \mathbf{R}^T \sqrt{\mathbf{\Sigma}_m}$. Then, the asymptotic MPV of S_e could be minimized through Eq. (20)

$$S_e = \frac{d - d^{'}}{(n-m) N_f} \tag{22}$$

which is non-negative (because $d - d^{'} \geq 0$) and directly computable. In the general case, $(d - d^{'})$ reflects the spectral contribution in the measured response that cannot be accounted for by the mode shape subspace.

(b) *Minimization with respect to* $\mathbf{R}$

In the previous Bayesian methods [30, 28], the MPV of the mode shapes was estimated using the Lagrange method under the normalization constraint. However, this requires proper selection of initial mode shapes so as to achieve the desired convergence to global minimal. To circumvent

the difficulty in providing a good initial guess of closely spaced mode shapes, we formulate the MPV search of the mode shapes as a JAD problem.

To do so, we first restrict the goal function (20) to the case with only one frequency f_k (i.e., $N_f = 1$) so that the following is involved

$$L_k = \ln|\mathbf{E}_k'| + \hat{\mathbf{F}}_k^* \mathbf{U}_m \mathbf{E}_k'^{-1} \mathbf{U}_m^T \hat{\mathbf{F}}_k. \tag{23}$$

where other terms are omitted because they are irrelevant to $\mathbf{R}$. Then, variation of the goal function L_k with respect to variation of $\mathbf{R}$ is found to be

$$\begin{aligned}
\delta L_k &= \delta(-\ln|\mathbf{E}_k'^{-1}| + \hat{\mathbf{F}}_k^* \mathbf{U}_m \mathbf{E}_k'^{-1} \mathbf{U}_m^T \hat{\mathbf{F}}_k) \\
&= \text{Re tr}(-\mathbf{E}_k' \delta \mathbf{E}_k'^{-1} + \mathbf{U}_m^T \hat{\mathbf{F}}_k \hat{\mathbf{F}}_k^* \mathbf{U}_m \delta \mathbf{E}_k'^{-1}) \\
&= -\text{tr}((\mathbf{U}_m^T \text{Re}(\hat{\mathbf{F}}_k \hat{\mathbf{F}}_k^*) \mathbf{U}_m - \mathbf{E}_k') \mathbf{E}_k'^{-1} \delta \mathbf{E}_k' \mathbf{E}_k'^{-1}) \\
&= -\text{tr}(\mathbf{E}_k'^{-1} (\mathbf{U}_m^T \text{Re}(\hat{\mathbf{F}}_k \hat{\mathbf{F}}_k^*) \mathbf{U}_m - \mathbf{E}_k') \mathbf{E}_k'^{-1} (\sqrt{\boldsymbol{\Sigma}_m} \delta \mathbf{R} \mathbf{H}_k \mathbf{R}^T \sqrt{\boldsymbol{\Sigma}_m} + \sqrt{\boldsymbol{\Sigma}_m} \mathbf{R} \mathbf{H}_k \delta \mathbf{R}^T \sqrt{\boldsymbol{\Sigma}_m})) \\
&= -2\text{tr}(\mathbf{H}_k \mathbf{R}^T \sqrt{\boldsymbol{\Sigma}_m} \mathbf{E}_k'^{-1} (\mathbf{U}_m^T \text{Re}(\hat{\mathbf{F}}_k \hat{\mathbf{F}}_k^*) \mathbf{U}_m - \mathbf{E}_k') \mathbf{E}_k'^{-1} \sqrt{\boldsymbol{\Sigma}_m} \delta \mathbf{R})
\end{aligned} \tag{24}$$

where δ is the variation operator and $\text{tr}(\cdot)$ denotes the trace of a matrix. Then, minimization of L_k with respect to $\mathbf{R}$ yields

$$\frac{\partial L_k}{\partial \mathbf{R}} = -2 \left(\mathbf{H}_k \mathbf{R}^T \sqrt{\boldsymbol{\Sigma}_m} \mathbf{E}_k'^{-1} (\mathbf{U}_m^T \text{Re}(\hat{\mathbf{F}}_k \hat{\mathbf{F}}_k^*) \mathbf{U}_m - \mathbf{E}_k') \mathbf{E}_k'^{-1} \sqrt{\boldsymbol{\Sigma}_m} \right) = \mathbf{0} \tag{25}$$

or more simply

$$\begin{aligned}
&\mathbf{U}_m^T \text{Re}(\hat{\mathbf{F}}_k \hat{\mathbf{F}}_k^*) \mathbf{U}_m = \mathbf{E}_k' \\
&\Rightarrow \boldsymbol{\Sigma}_m^{-1/2} \mathbf{U}_m^T (\text{Re}(\hat{\mathbf{F}}_k \hat{\mathbf{F}}_k^*) - S_e \mathbf{I}_n) \mathbf{U}_m \boldsymbol{\Sigma}_m^{-1/2} = \mathbf{R} \mathbf{H}_k \mathbf{R}^T \\
&\Rightarrow \mathbf{H}_k = \mathbf{R}^{-1} \boldsymbol{\Lambda}_k \mathbf{R}^{-T}
\end{aligned} \tag{26}$$

where $\boldsymbol{\Lambda}_k = \boldsymbol{\Sigma}_m^{-1/2} \mathbf{U}_m^T (\text{Re}(\hat{\mathbf{F}}_k \hat{\mathbf{F}}_k^*) - S_e \mathbf{I}_n) \mathbf{U}_m \boldsymbol{\Sigma}_m^{-1/2}$ is directly computable and $\mathbf{H}_k$, as is assumed in the preceding, is a diagonal and real matrix. To see more, summation of (26) from $k = 1$ to $k = N_f$ yields

$$\begin{aligned}
\sum_{k=1}^{N_f} \mathbf{H}_k &= \mathbf{R}^{-1} \sum_{k=1}^{N_f} \boldsymbol{\Lambda}_k \mathbf{R}^{-T} \\
&= \mathbf{R}^{-1} \boldsymbol{\Sigma}_m^{-1/2} \mathbf{U}_m^T (\mathbf{D} - N_f S_e \mathbf{I}_n) \mathbf{U}_m \boldsymbol{\Sigma}_m^{-1/2} \boldsymbol{\Lambda}_k \mathbf{R}^{-T} \\
&= \mathbf{R}^{-1} (\mathbf{I}_m - S_e (\boldsymbol{\Sigma}_m / N_f)^{-1}) \mathbf{R}^{-T} \approx \mathbf{R}^{-1} \mathbf{R}^{-T}
\end{aligned} \tag{27}$$

where $\mathbf{D}$ is defined in Eq. (13) and the approximation in the last step holds for high signal to noise ratio. For normalization, we can firstly assume that $\mathbf{R}$ is an othonormal matrix so that $\sum_{k=1}^{N_f} \mathbf{H}_k \approx \mathbf{R}^{-1} \mathbf{R}^{-T} = \mathbf{I}$. Considering the othonormal matrix $\mathbf{R}$ and the N_f eigen equations (26), a joint approximate diagonalization (JAD) problem [36, 14] can be quickly formulated,

$$\begin{aligned}
&\text{minimize } \text{J}_{\text{AD}}(\mathbf{R}; \{\boldsymbol{\Lambda}_k\}_{k=1}^{N_f}) = \sum_{k=1}^{N_f} \text{off}(\mathbf{R}^{-1} \boldsymbol{\Lambda}_k \mathbf{R}^{-T}) = \sum_{k=1}^{N_f} \text{off}(\mathbf{R}^T \boldsymbol{\Lambda}_k \mathbf{R}) \\
&\text{subject to } \mathbf{R}^T \mathbf{R} = \mathbf{I}_m
\end{aligned} \tag{28}$$

where $\text{off}(\mathbf{B}) = \sum_{1 \le i \ne j \le m} |(\mathbf{B})_{ij}|^2$ collects the squares of off-diagonal elements of the $m \times m$ matrix $\mathbf{B}$ and $(\mathbf{B})_{ij}$ is the (i, j)-entry of $\mathbf{B}$. The JAD problem has been largely investigated in the literature [14] and many algorithms have been developed. In this paper, the well-known Jacobi rotation algorithm [14] is adopted to solve the JAD problem (28) and the details are

presented in Table 1. Note in the algorithmic table that $\{\mathbf{\Lambda}_k\}_{k=1}^{N_f}$ are real symmetric matrices so that $z = 0$ in the unit normal eigenvector of $\mathbf{G}$, s is a real number and then, $\mathbf{R}_o$ as well as the output matrix $\mathbf{R}$ is a real matrix. Once $\mathbf{R}$ is obtained by solving the JAD problem, the mode shapes will be identified from Eq. (15),

$$\hat{\mathbf{\Phi}} = \mathbf{U}_m\sqrt{\mathbf{\Sigma}_m}\mathbf{R} = \left[\hat{\phi}_1, \hat{\phi}_2, \ldots, \hat{\phi}_m\right] \tag{29}$$

where $||\hat{\phi}_j|| = ||\mathbf{U}_m\sqrt{\mathbf{\Sigma}_m}\mathbf{r}_j|| = \sqrt{\mathbf{r}_j^T\mathbf{\Sigma}_m\mathbf{r}_j}$ is not normalized and $\mathbf{r}_j$ is the jth-column of the matrix $\mathbf{R}$. To get the desired normalized mode shapes, $\mathbf{R}$ should be further re-normalized as

$$\mathbf{R} = \left[\frac{\mathbf{r}_1}{\sqrt{\mathbf{r}_1^T\mathbf{\Sigma}_m\mathbf{r}_1}}, \frac{\mathbf{r}_2}{\sqrt{\mathbf{r}_2^T\mathbf{\Sigma}_m\mathbf{r}_2}}, \ldots, \frac{\mathbf{r}_m}{\sqrt{\mathbf{r}_m^T\mathbf{\Sigma}_m\mathbf{r}_m}}\right] \tag{30}$$

and then, the eventual mode shapes are identified as $\mathbf{\Phi} = \mathbf{U}_m\sqrt{\mathbf{\Sigma}_m}\mathbf{R}$.

Table 1: Pseudo-codes of Jacobi rotation algorithm to solve the JAD problem (28)

Inputs:
Load the input matrices $\mathbf{\Lambda}_k, k = 1, ..., N_f$ (all of size $m \times m$).
Set threshold ϵ_s (e.g.,=10^{-8});
Initialize $\mathbf{R} = \mathbf{I}_m$;

Jacobi rotation:
While $|s| \geq \epsilon_s$
  for $i = 1 : m-1$
    for $j = i+1 : m$
      $\mathbf{v}_k = [(\mathbf{\Lambda}_k)_{ii} - (\mathbf{\Lambda}_k)_{jj}, (\mathbf{\Lambda}_k)_{ij} + (\mathbf{\Lambda}_k)_{ji}, \mathrm{i}((\mathbf{\Lambda}_k)_{ji} - (\mathbf{\Lambda}_k)_{ij}))], k = 1, 2, ..., N_f$;
      $\mathbf{G} = \sum_{k=1}^{N_f}\mathbf{v}_k^T\mathbf{v}_k$;
      $[x, y, z]^T$ (with $x \geq 0$) is the normalized eigenvector of $\mathbf{G}$ with maximum eigenvalue;
      $c = \sqrt{\frac{1+x}{2}}, s = \frac{y-\mathrm{i}z}{2c}$;
      $\mathbf{R}_o = \mathbf{0}_{m\times m}$ and fill in $(\mathbf{R}_o)_{ii} = (\mathbf{R}_o)_{jj} = c, (\mathbf{R}_o)_{ij} = \bar{s}, (\mathbf{R}_o)_{ji} = -s$;
      Update $\mathbf{R} \leftarrow \mathbf{R}\mathbf{R}_o^*$;
      Update $\mathbf{\Lambda}_k \leftarrow \mathbf{R}_o\mathbf{\Lambda}_k\mathbf{R}_o^*, k = 1, 2, ..., N_f$;
    end
  end
end

Outputs: $\mathbf{R}$.

3.2 Stage 2: Newton iteration to get modal frequencies and damping ratios

In the second stage, the MPV of the remaining natural frequencies, damping ratios and modal force PSD $(\mathbf{f}, \zeta, \mathbf{S})$ are to be derived. These parameters are all contained in $\{\mathbf{H}_k\}_{k=1}^{N_f}$. By considering $\mathbf{E}_k' \approx \sqrt{\mathbf{\Sigma}_m}\mathbf{R}\mathbf{H}_k\mathbf{R}^T\sqrt{\mathbf{\Sigma}_m}$ under high signal to noise ratio, the goal function in Eq. (20) is further simplified in terms of $\{\mathbf{H}_k\}_{k=1}^{N_f}$ to

$$L(\theta) = \sum_{k=1}^{N_f}\ln|\mathbf{H}_k| + \sum_{k=1}^{N_f}\mathrm{tr}(\mathbf{H}_k^{-1}\mathbf{A}_k) \tag{31}$$

where $\mathbf{A}_k = \mathbf{R}^{-1}\mathbf{\Sigma}_m^{-1/2}\mathbf{U}_m^T \mathrm{Re}(\hat{\mathbf{F}}_k\hat{\mathbf{F}}_k^*)\mathbf{U}_m\mathbf{\Sigma}_m^{-1/2}\mathbf{R}^{-T}$ is computable with $\mathbf{R}$ given in Eq. (30). Other terms in the equation are independent from $\{\mathbf{H}_k\}_{k=1}^{N_f}$ and thus, are omitted. As was analyzed at the beginning of Section 3, $\{\mathbf{H}_k\}_{k=1}^{N_f}$ are assumed to be diagonal and then, only the diagonal part of $\mathbf{S}$, designated as $\mathrm{diag}(S_{11}, S_{22}, ..., S_{mm})$, will contribute and be considered for optimization herein. Considering this, the diagonal elements of $\mathbf{H}_k$ are

$$(\mathbf{H}_k)_{ii} = |h_{ik}|^2 S_{ii} = \frac{S_{ii}\,(2\pi f_k)^{-2q}}{(1-(f_i/f_k)^2)^2 + (2\zeta_i f_i/f_k)^2}, i = 1, 2, ..., m \tag{32}$$

with h_{ik} defined in Eq. (4), and the goal function further becomes

$$L(\boldsymbol{\theta}) = \sum_{i=1}^{m}\sum_{k=1}^{N_f}\left(\ln(\mathbf{H}_k)_{ii} + (\mathbf{H}_k)_{ii}^{-1}(\mathbf{A}_k)_{ii}\right). \tag{33}$$

To simplify, set

$$a_i = \frac{1}{S_{ii}}, \quad b_i = \frac{(4\zeta_i^2 - 2)f_i^2}{S_{ii}}, \quad c_i = \frac{f_i^4}{S_{ii}} \tag{34}$$

and then, $(\mathbf{H}_k)_{ii}^{-1} = a_i\,(2\pi f_k)^{2q} + b_i\,(2\pi f_k)^{2q}/f_k^2 + c_i\,(2\pi f_k)^{2q}/f_k^4$. In this way, Eq. (33) turns into

$$\begin{aligned} L(\boldsymbol{\theta}) = \sum_{i=1}^{m}\Bigg(&-\sum_{k=1}^{N_f}\ln\left(a_i\,(2\pi f_k)^{2q} + b_i\frac{(2\pi f_k)^{2q}}{f_k^2} + c_i\frac{(2\pi f_k)^{2q}}{f_k^4}\right) \\ &+a_i\sum_{k=1}^{N_f}(\mathbf{A}_k)_{ii}\,(2\pi f_k)^{2q} + b_i\sum_{k=1}^{N_f}\frac{(\mathbf{A}_k)_{ii}\,(2\pi f_k)^{2q}}{f_k^2} + c_i\sum_{k=1}^{N_f}\frac{(\mathbf{A}_k)_{ii}\,(2\pi f_k)^{2q}}{f_k^4}\Bigg) \end{aligned} \tag{35}$$

where once the optimal values of (a_i, b_i, c_i) are obtained, the modal parameters are quickly identified as

$$S_{ii} = \frac{1}{a_i}, f_i = \left(\frac{c_i}{a_i}\right)^{1/4}, \zeta_i = \frac{1}{2}\sqrt{2 + \frac{b_i}{a_i f_i^2}}, i = 1, 2, ..., m. \tag{36}$$

By designating $\mathbf{u}_k = [(2\pi f_k)^{2q}, (2\pi f_k)^{2q}/f_k^2, (2\pi f_k)^{2q}/f_k^4]^T$, minimization of Eq. (35) with respect to (a_i, b_i, c_i) yields

$$\sum_{k=1}^{N_f}\mathbf{u}_k\frac{1}{\mathbf{u}_k^T\cdot[a_i, b_i, c_i]^T} = \sum_{k=1}^{N_f}(\mathbf{A}_k)_{ii}\mathbf{u}_k, i = 1, 2, ..., m \tag{37}$$

and the Newton iteration can be used to solve this equation. Specifically, at the jth iteration step, the solution is updated in the following way

$$\begin{aligned} &\left(\sum_{k=1}^{N_f}\frac{\mathbf{u}_k\mathbf{u}_k^T}{(\mathbf{u}_k^T\cdot[a_i^{(j-1)}, b_i^{(j-1)}, c_i^{(j-1)}]^T)^2}\right)\left(\begin{bmatrix} a_i^{(j)} \\ b_i^{(j)} \\ c_i^{(j)} \end{bmatrix} - \begin{bmatrix} a_i^{(j-1)} \\ b_i^{(j-1)} \\ c_i^{(j-1)} \end{bmatrix}\right) \\ &= \sum_{k=1}^{N_f}\mathbf{u}_k\left(\frac{1}{\mathbf{u}_k^T\cdot[a_i^{(j-1)}, b_i^{(j-1)}, c_i^{(j-1)}]^T} - (\mathbf{A}_k)_{ii}\right), i = 1, 2, ..., m \end{aligned} \tag{38}$$

where $[a_i^{(j-1)}, b_i^{(j-1)}, c_i^{(j-1)}]$ is prescribed in the previous $(j-1)$th step and $[a_i^{(j)}, b_i^{(j)}, c_i^{(j)}]$ can be obtained by solving the linear equation (38). By iteration, the final solution is obtained when the convergence criterion is satisfied. A noteworthy thing regarding the Newton iteration is that a proper initial guess $[a_i^{(0)}, b_i^{(0)}, c_i^{(0)}]$ should be prescribed in order for fast convergence. To do so, the initial

natural frequency $f_i^{(0)}$ can be quickly determined at the peak of the spectrum curve, the initial damping ratio is assigned to $\zeta_i^{(0)} = 1\%$ and the initial modal force PSD $S_{ii}^{(0)}$ is estimated by minimizing Eq. (33) with respect to S_{ii} as

$$S_{ii}^{(0)} = \frac{\sum_{k=1}^{N_f} (\mathbf{A}_k)_{ii} / |h_{ik}^{(0)}|^2}{N_f} \tag{39}$$

where $|h_{ik}^{(0)}|^2 = \frac{(2\pi f_k)^{-2q}}{(1-(f_i^{(0)}/f_k)^2)^2 + \left(2\zeta_i^{(0)} f_i^{(0)}/f_k\right)^2}$. With initial $(f_i^{(0)}, \zeta_i^{(0)}, S_{ii}^{(0)})$, the initial $[a_i^{(0)}, b_i^{(0)}, c_i^{(0)}]$ is quickly determined by resorting to Eq. (34).

To conclude, the modal frequencies and damping ratios are identified in Stage 2 through Newton iteration. Such iteration not only decouples with the optimization over the mode shapes, but also proceeds independently for the m different modes (or different $i \in \{1, 2, ..., m\}$), each involving a three-parameter optimization problem. Thus, it is easily deduced that the proposed two-stage method would be more efficient than conventional Bayesian methods.

Eventually, the algorithmic details of the proposed two-stage method for modal parameter identification with closely spaced modes are outlined in Table 2.

Table 2: Algorithmic details of two-stage method for searching the MPV of the NLLF

Inputs:
– Load the time history data $\hat{\mathbf{y}}_j$ or its Fourier transform $\hat{\mathbf{F}}_k$,
– Define the error tolerance *tol* (e.g.,=10^{-6}) and the maximum iteration number N_{max} (e.g.,=1000),

Stage 1: Identify $\mathbf{\Phi}$ and S_e
– Get $\mathbf{U}_m$ and $\mathbf{\Sigma}_m$ through SVD of $\mathbf{D}$ as in Eqs. (12) and (14),
– Estimate S_e through Eq. (22),
– Calculate $\mathbf{\Lambda}_k = \mathbf{\Sigma}_m^{-1/2} \mathbf{U}_m^T (\mathrm{Re}(\hat{\mathbf{F}}_k \hat{\mathbf{F}}_k^*) - S_e \mathbf{I}_n) \mathbf{U}_m \mathbf{\Sigma}_m^{-1/2}$,
– Proceed JAD of $\mathbf{\Lambda}_k$ through the Jacobi rotation algorithm in Table 1 to get the matrix $\mathbf{R}$,
– Obtain the mode shapes $\mathbf{\Phi}$ as in Eq. (15),
Outputs: $\mathbf{\Phi}$ and S_e

Stage 2: Search for $f_i, \zeta_i, S_{ii}, i = 1, 2, ..., m$
– Initially set $f_i^{(0)}$ as the peak frequency of spectrum curve, $\zeta_i^{(0)} = 1\%$, and $S_{ii}{}^{(0)}$ via Eq. (39),
– Get the initial $a_i^{(0)}, b_i^{(0)}, c_i^{(0)}$ as in Eq. (34),
– Calculate $\mathbf{A}_k = \mathbf{R}^{-1} \mathbf{\Sigma}_m^{-1/2} \mathbf{U}_m^T \mathrm{Re}(\hat{\mathbf{F}}_k \hat{\mathbf{F}}_k^*) \mathbf{U}_m \mathbf{\Sigma}_m^{-1/2} \mathbf{R}^{-T}$,
- **for** $j = 1 : N_{max}$
  - Update $a_i^{(j)}, b_i^{(j)}, c_i^{(j)}, i = 1, 2, ..., m$ through Eq. (38),
  - if $\left\{ \left\| a_i^{(j)} - a_i^{(j-1)} \right\|_2 / \left\| a_i^{(j)} \right\|_2, \left\| b_i^{(j)} - b_i^{(j-1)} \right\|_2 / \left\| b_i^{(j)} \right\|_2, \left\| c_i^{(j)} - c_i^{(j-1)} \right\|_2 / \left\| c_i^{(j)} \right\|_2 \right\} \leq tol$, break.
- **end**
- Compute the eventual f_i, ζ_i, S_{ii} through Eq. (36),
Outputs: $f_i, \zeta_i, S_{ii}, i = 1, 2, ..., m$

4 Numerical example

To assess the effectiveness and efficiency of the proposed two-stage method for identifying closely spaced modes within the Bayesian FFT framework, empirical investigations are presented herein using synthetic data. The synthetic data example serves to assess the method's consistency. The first set of examples utilized synthetic data to verify the effectiveness of the proposed method under different closeness of the two modes. The second set of examples demonstrates its performance under three

closely spaced modes. For comparative purposes, we also present results obtained using the PX-EM algorithm, as described in [30].

4.1 Synthetic data for two closely spaced modes

The synthetic data is generated by considering two closely spaced modes and three measurement channels at a sampling rate of 100 Hz and a duration of 600 s. The data is expressed as

$$\hat{\mathbf{y}}_j = \phi_1 \ddot{\eta}_1(t_j) + \phi_2 \ddot{\eta}_2(t_j) + \varepsilon(t_j), \tag{40}$$

where $\varepsilon(t_j)$ are the random noises, pertaining to the Gaussian distribution and being independently sampled at different time instants t_j. $\ddot{\eta}_i(t_j)(i = 1, 2)$ is the modal acceleration response, satisfying the governing equation

$$\ddot{\eta}_i(t) + 2\zeta_i\omega_i\dot{\eta}_i(t) + \omega_i^2\eta_i(t) = p_i(t) \tag{41}$$

with natural frequencies of $\omega_i = 2\pi f_i$, $f_1 = 1$Hz, $f_2 = 1.02$Hz and damping ratios $\zeta_1 = 1\%, \zeta_2 = 1.5\%$. The modal excitations $p_i(t)(i = 1, 2)$ are modelled as stationary Gaussian white noise with PSD $S_{11} = S_{22} = 1\mu g^2/$Hz, and cross PSD $S_{12} = 0.1e^{\mathrm{i}\pi/4}\mu g^2/$Hz. The prediction error PSD S_e are set to $10\mu g^2/$Hz. The mode shapes are given by

$$\phi_1 = [1, 2, 2]^T/3, \phi_2 = [-2, 1, 2]^T/3. \tag{42}$$

For illustration, Figure 9 plots the singular values of the response PSD matrix at different frequencies. This plot not only provides a rough idea of natural frequencies around 1 Hz at the peak of the spectrum curve, but also indicates that there are two closely spaced modes around 1 Hz because in the vicinity of this frequency, the first two singular values are significantly larger than the third singular value. Moreover, from the figure, a frequency band of $[0.8, 1.2]$ Hz is reasonably selected for later Bayesian FFT analysis and the peak frequencies of the first two singular values are used as the initial guess of the two close frequencies in later iterative search of the MPVs. Table 3 presents the identified modal parameters for closely spaced modes, alongside their corresponding exact values where the MAC is calculated between the identified and exact mode shapes. Herein, the values in the brackets represent the coefficient of variation (c.o.v) of the identified parameters and the definition throughout this paper is given as follows:

- For identified natural frequencies, damping ratios, modal force PSD and prediction error PSD, the c.o.v is defined as ratio of the standard deviation to the mean, that is,

$$\text{c.o.v} = \frac{\sigma_\theta}{\mu_\theta} \tag{43}$$

  where μ_θ the mean or MPV and σ_θ the standard deviation of the identified parameter;

- For identified mode shapes, the c.o.v of the MAC for mode shapes is defined as the trace of the posterior covariance matrix [29].

The singular values of the response PSD matrices at different frequencies are plotted in Figure 9, with the analysis frequency range spanning from 0.8 Hz to 1.2 Hz. It is important to note that the spectral density plot in Figure 9 shows the coupling of two closely spaced modes, which complicates the identification of the initial frequency points. The two resonance frequencies selected from the plot are 1.001 Hz and 1.0071 Hz, which differ significantly from the true values of 1 Hz and 1.02 Hz, respectively. This highlights the difficulty of selecting accurate frequencies in closely spaced modes problems.

Table 3 presents the identified modal parameters for closely spaced modes, the comparison in the table reveals that the identified values for proposed method are very close to the exact values.

Notably, the two natural frequencies exhibit a low c.o.v around 0.19% and 0.17% for both methods respectively. In terms of the damping ratios, the c.o.v stands at approximately 11.76% for the PX-EM method and 19.83% for the proposed method in the first mode. This result indicates that identifying damping ratios is associated with greater uncertainty compared to natural frequency identification. As for the mode shapes, the proposed method clearly outperforms the PX-EM method, as indicated by the higher MAC values (or closer to 1) and lower uncertainty coefficients. In terms of modal force PSD, the c.o.v is 0.12%, which is of similar magnitude to that of the damping ratios.

Table 3: Modal parameters identification results, including the means and the c.o.v (in brackets) for synthetic data with two close frequencies (f_1=1 Hz and f_2=1.02Hz). The CPU time and Iteration numbers to calculate the MPVs are also presented.

Parameter		Mode 1	Mode 2
Natural frequency f_i[Hz]	Exact	1	1.02
	Initial value	1.001	1.0071
	PX-EM	1.0084(0.0019)	1.0092(0.0019)
	Proposed	1.0040(0.0017)	1.0208(0.0023)
Damping ratio ζ_i[%]	Exact	1	1.5
	Initial value	1	1
	PX-EM	1.31(0.1177)	1.33(0.1176)
	Proposed	0.87(0.1983)	1.55(0.1747)
Mode shape MAC	PX-EM	0.5063(0.2938)	0.1643(0.3333)
	Proposed	0.9990(0.0658)	0.9994(0.0948)
Modal force PSD $\mathbf{S}$	Exact	1	1
	PX-EM	183.75(6.4867)	177.25(6.6057)
	Proposed	1.1382(0.1248)	1.1286(0.1575)
Prediction error PSD S_e	Exact	10	
	PX-EM	10.40(0.0586)	
	Proposed	10.58(0.0597)	
	CPU time to calculate the MPVs		
PX-EM	1.79s		
Proposed	0.06s		
	Number of iterations	NLLF value	
PX-EM	39	3512	
Proposed	6	3509.4	

For the PX-EM method, the selection of initial values is especially critical. The choice of initial frequency not only directly impacts the frequency iteration results but also influences the estimation of the initial modes in Eq. (12). It can be observed from Table 4 that when the initial guess of frequencies are selected to be exact frequencies $f_1 = 1$ Hz, $f_2 = 1.02$ Hz, the PX-EM method provides more reasonable results with MAC above 0.95 for both modes compared to cases where the initial guess for frequencies are selected to be observed frequency peaks. This is also reflect on the number of iterations required, which reduces from 39 to 22. In contrast, for the proposed method, the impact of initial frequency values is almost negligible. This is because the JAD method does not require an initial estimate of mode shapes and the identification of natural frequencies and damping ratios in Stage 2 is less sensitive to initial guess of frequencies. As a consequence, the proposed method is found quite less sensitive to initial guesses of modal parameters, giving rise to more robust results .

Additionally, the proposed method is shown to be more efficient than the PX-EM method through Tables 3 and 4, which compares the computation time (using MATLAB on an Intel(R) Core(TM)

Table 4: Modal parameters identification results, including the means and the c.o.v (in brackets) for synthetic data with two close frequencies (f_1=1 Hz and f_2=1.02Hz). The exact natural frequencies are used as initial guess of frequencies. The CPU time and Iteration numbers to calculate the MPVs as well as the eventual NLLF value is also presented

Parameter		Mode 1	Mode 2
Natural frequency f_i[Hz]	Exact	1	1.02
	Initial value	1	1.02
	PX-EM	1.0017(0.0018)	1.0178(0.0024)
	Proposed	1.0040(0.0017)	1.0208(0.0023)
Damping ratio ζ_i[%]	Exact	1	1.5
	Initial value	1	1
	PX-EM	0.96(0.1913)	1.41(0.1607)
	Proposed	0.87(0.1983)	1.55(0.1747)
Mode shape MAC	PX-EM	0.9867(0.1071)	0.9561(0.1695)
	Proposed	0.9990(0.0658)	0.9994(0.0948)
	CPU time to calculate the MPVs		
PX-EM	1.34s		
Proposed	0.06s		
	Number of iterations		NLLF value
PX-EM	22		3503
Proposed	6		3509.4

i9-7920X processor) for calculating the MPVs, as well as the number of steps required to achieve convergence for both methods. Clearly, the proposed method requires less iterations and CPU time. This superiority in efficiency is mainly attributed to the decoupling property of the proposed method where the mode shapes and natural frequencies/damping ratios are identified in two sequential stages. Moreover, the convergence of the NLLF corresponding to the results in Table 3 is graphically illustrated in Figure 2. The eventual NLLF of the proposed method is (slightly) less than that of the PX-EM method, again demonstrates the better accuracy achieved by the proposed method.

As is well known, closer frequencies make it harder to accurately identify modal parameters. To investigate the performance of the proposed method under different closeness of the closely spaced modes, the second frequency f_2 is further considered to vary in a range from 1.007 to 1.075 Hz, while the first frequency is fixed at $f_1 = 1$ Hz. In this way, the frequency separation $\Delta f = f_2 - f_1$ varies from 0.007 to 0.075 Hz. The identification results under different frequency separations Δf are schematically exhibited in Figures 3–8 and some of them are specifically listed in Table 5 for reference.

Table 5: Modal parameters identification results including the means and the c.o.v (in brackets) for synthetic data under different frequency separations Δf. MAC 1 and MAC 2 represent the MAC values of the first and second mode shapes respectively.

Parameter	f_1	f_2	ζ_1	ζ_2	MAC 1	MAC 2
PX-EM($\Delta f = 0.007$)	1.0018(0.0021)	1.0025(0.0022)	1.15(0.1944)	1.20(0.1904)	0.9059(0.0566)	0.6350(0.0524)
Proposed($\Delta f = 0.007$)	1.0033(0.0011)	1.0059(0.0026)	0.97(0.1198)	1.26(0.2580)	0.9467(0.1055)	0.9567(0.2175)
PX-EM($\Delta f = 0.011$)	1.0008(0.0017)	1.0091(0.0028)	0.80(0.2180)	1.99(0.1775)	0.9796(0.0635)	0.9368(0.0525)
Proposed($\Delta f = 0.011$)	1.0019(0.0016)	1.0098(0.0031)	0.78(0.2056)	2.30(0.1676)	0.9875(0.0784)	0.9777(0.1524)
PX-EM($\Delta f = 0.017$)	1.0025(0.0019)	1.0186(0.0018)	1.07(0.1875)	0.99(0.1933)	0.9875(0.0852)	0.9999(0.0871)
Proposed($\Delta f = 0.017$)	1.0038(0.0019)	1.0201(0.0018)	1.01(0.1927)	1.06(0.1841)	0.9996(0.0934)	0.9986(0.0881)
PX-EM($\Delta f = 0.035$)	1.0004(0.0020)	1.0335(0.0023)	1.17(0.1771)	1.53(0.1628)	0.9802(0.0644)	0.9967(0.0706)
Proposed($\Delta f = 0.035$)	1.0017(0.0018)	1.0358(0.0022)	0.98(0.1880)	1.43(0.1693)	0.9870(0.0526)	0.9903(0.0469)

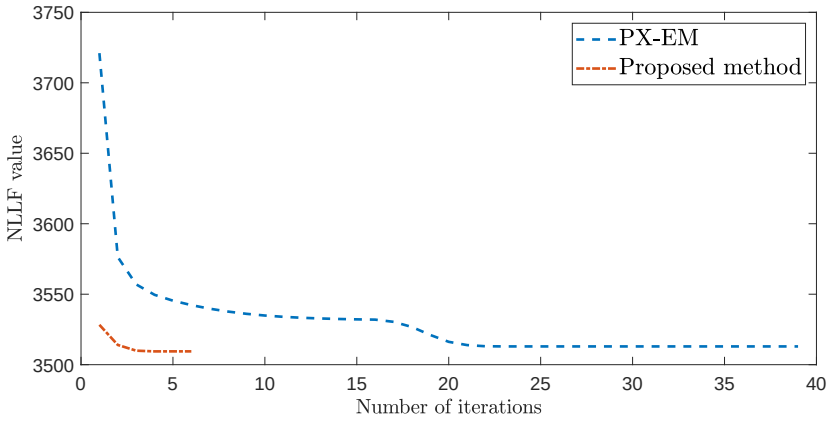

Figure 2: Iteration of NLLF values for two closely spaced modes using PX-EM and the proposed method

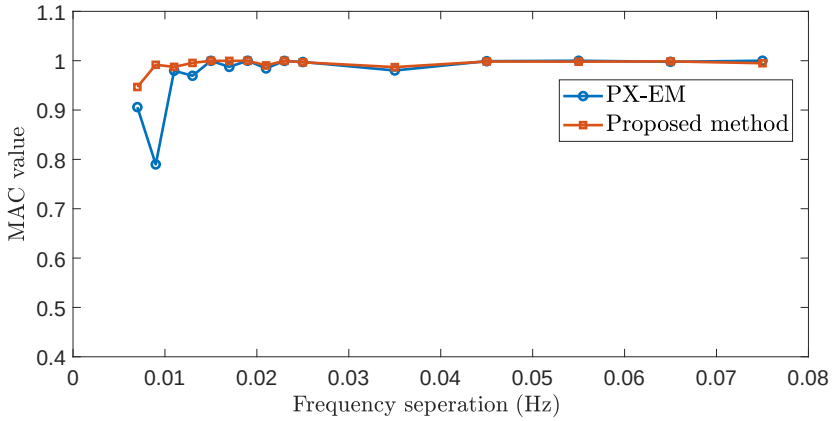

Figure 3: MAC values of the first identified mode shape for synthetic data under different frequency separations Δf

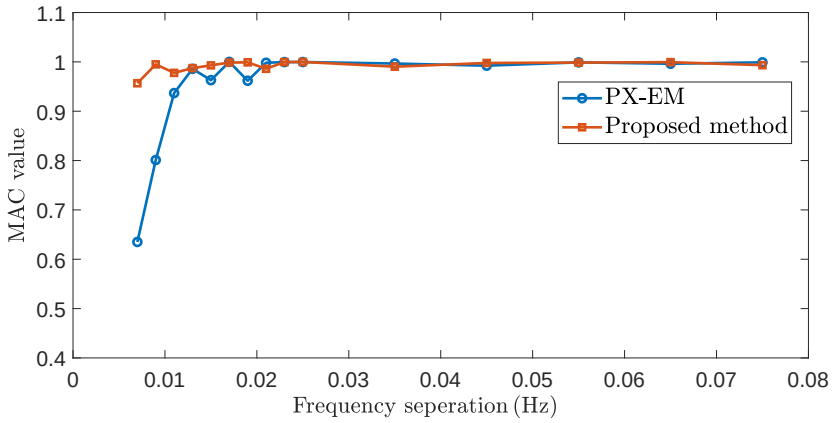

Figure 4: MAC values of the second identified mode shape for synthetic data under different frequency separations Δf

Figures 3 and 4 show the MAC values of the two identified mode shapes by the two methods under different frequency separations Δf. As can be observed from the figures, both methods give satisfactory identification of the mode shapes with the MAC exceeding 0.99 when the two modes are relatively well separated with $\Delta f \geq 0.035$ Hz. However, the accuracy in the identified mode shapes by the PX-EM method substantially degrades when $\Delta f \leq 0.025$ Hz and the degradation in the second mode, with the MAC even less than 0.7, is more evident than that in the first mode. This is because, in the case of two close frequencies, one mode dominates while the other is weaker. During the initial estimation of mode shapes in the PX-EM method, the weaker mode is influenced by the stronger one, affecting the identification results. While by the proposed method, the first two modes MAC is all greater than 0.97, giving clearly better identification of mode shapes than the PX-EM method when the two modes are very close with $\Delta f \leq 0.025$ Hz.

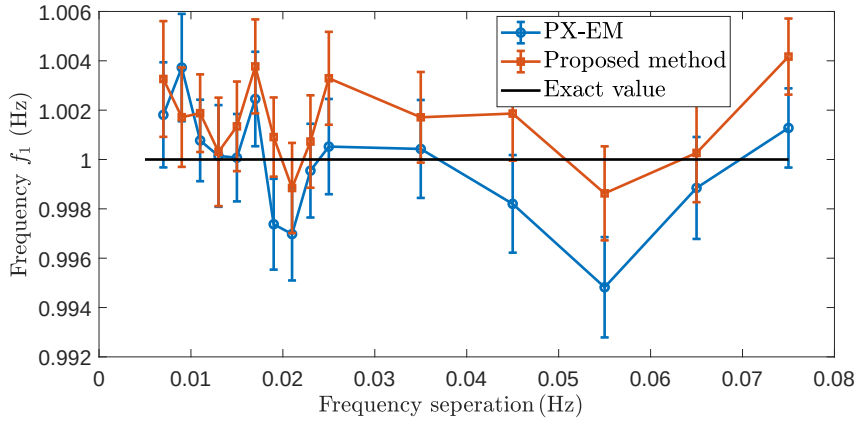

Figure 5: Identification results including the mean and standard deviation of the first natural frequency f_1 for synthetic data under different frequency separations Δf

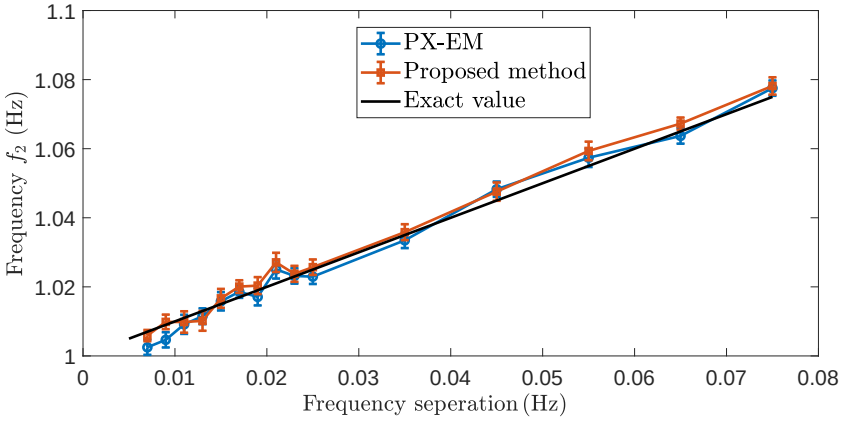

Figure 6: Identification results including the mean and standard deviation of the second natural frequency f_2 for synthetic data under different frequency separations Δf

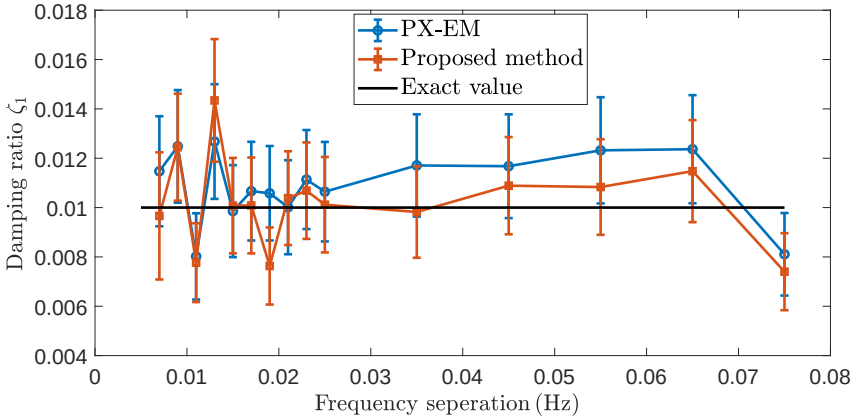

Figure 7: Identification results including the mean and standard deviation of the first mode damping ratio ζ_1 for synthetic data under different frequency separations Δf

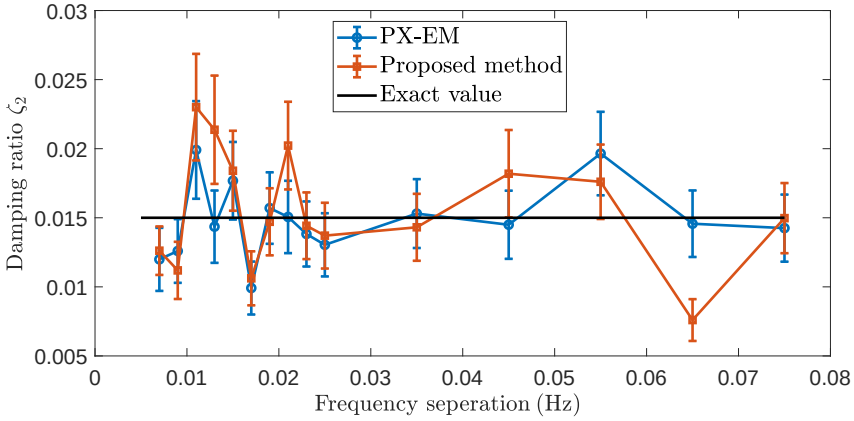

Figure 8: Identification results including the mean and standard deviation of the second mode damping ratio ζ_2 for synthetic data under different frequency separations Δf

Figures 5 and 6 display the identification results of the two frequencies f_1, f_2 under different frequency separations Δf. Both methods have given rise to satisfactory identification of the frequencies, because the relative errors are all less than 1%. Figures 7 and 8 present the identified damping ratios under different frequency separations Δf. When identifying the damping ratio, both methods perform similarly. Generally, damping ratios are difficult to identify, but the values identified by both methods fall within an acceptable range.

To conclude, the proposed method gives similarly good identification of natural frequencies and damping ratios to the PX-EM method. Nonetheless, in term of mode shape identification, the proposed method performs better than the PX-EM method, especially when the two modes are very closely spaced, e.g., $\Delta f \leq 0.025$ Hz. This also indicates that reformulating mode shape identification into the JAD problem is reasonable and well-posed. Additionally, the proposed method is found to be more efficient than the PX-EM method, due to the decoupling property of the two-stage solution strategy.

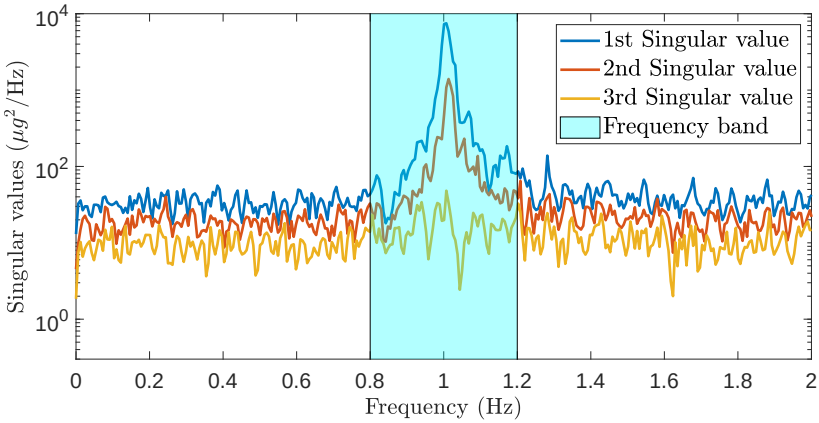

Figure 9: Singular values of response PSD for synthetic data with f_1=1 Hz, f_2=1.02 Hz

4.2 Synthetic data for three closely spaced modes

To validate the effectiveness of the proposed method for more closely spaced modes, we further use synthetic data generated by three closely spaced modes and three measurement channels sampled at the rate of 100 Hz and the duration of 600 s. The acceleration data is generated in a similar form to Eq. (40), but with three modes where the natural frequencies are $f_1 = 1$ Hz, $f_2 = 1.02$ Hz, $f_3 = 1.04$ Hz, the damping ratios are $\zeta_1 = 1\%$, $\zeta_2 = 1.2\%$, $\zeta_3 = 1.5\%$, $p_i(t)(i = 1, 2, 3)$ are modelled as stationary Gaussian white noise with PSD $S_{11} = S_{22} = S_{33} = 1\mu g^2/\text{Hz}$, and cross PSD $S_{12} = 0.1e^{\text{i}\pi/4}\mu g^2/\text{Hz}$, and the mode shapes are set to

$$\phi_1 = [1, 2, 2]^T/3, \phi_2 = [-2, 1, 2]^T/3, \phi_3 = [-1, 2, -1]^T/3. \tag{44}$$

The singular values of the response PSD matricies at different frequencies are plotted in Figure 10 where the frequency band for analysis is [0.8, 1.2] Hz. As is observed in the figure, the presence of three closely spaced modes around 1 Hz is well indicated by the fact that the first three singular values all increasing significantly within the resonant frequency band. Compared to the scenario with two close frequencies in Figure 9, the third singular value in this case clearly exhibits higher values. Therefore, the number of closely spaced modes can also be determined by counting the singular values, that have significantly higher values than the others.

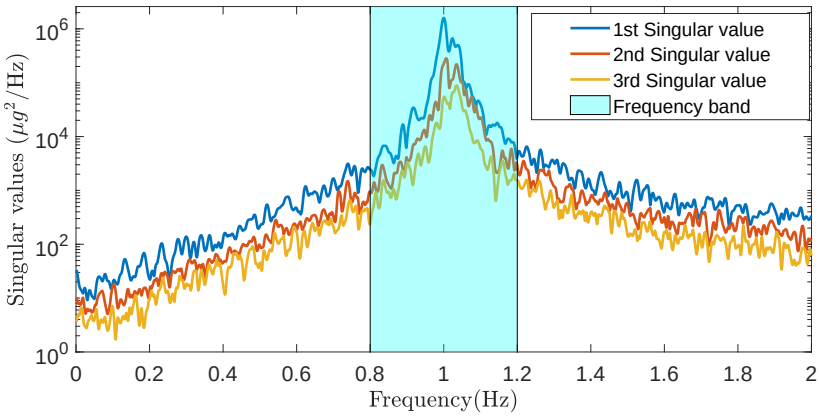

Figure 10: Singular values of response PSD for synthetic data with f_1=1 Hz, f_2=1.02 Hz and f_3=1.04 Hz

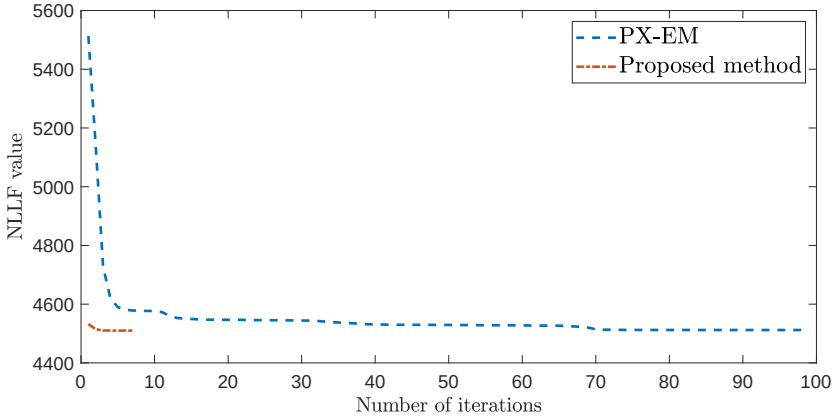

Figure 11: Iteration of NLLF values for three closely spaced modes using PX-EM and the proposed method

Table 6: Modal parameters identification results including the means and the c.o.v (in the brackets) for synthetic data with three close frequencies (f_1=1 Hz, f_2=1.02 Hz and f_3=1.04 Hz). The CPU time and Iteration numbers to calculate the MPVs as well as the eventual NLLF value is also presented.

Parameter		Mode 1	Mode 2	Mode 3
Frequency f_i[Hz]	Exact	1	1.02	1.04
	Initial value	1.001	1.0376	1.0489
	PX-EM	1.0009(0.0014)	1.0300(0.0024)	1.0325(0.0023)
	Proposed	1.000(0.0018)	1.0238(0.0029)	1.0402(0.0023)
Damping ratio ζ_i[%]	Exact	1	1.2	1.5
	Initial value	1	1	1
	PX-EM	0.61(0.2468)	1.81(0.1115)	1.78(0.1123)
	Proposed	0.95(0.2314)	1.75(0.1903)	1.81(0.1440)
Mode shape MAC	PX-EM	0.9935(0.3588)	0.5956(5.0571)	0.8123(5.1327)
	Proposed	0.9998(0.0798)	0.9898(0.1867)	0.9905(0.1085)
Modal force PSD $\mathbf{S}$	Exact	1	1	1
	PX-EM	0.9549(0.1364)	31.9807(2.3643)	31.6693(2.3764)
	Proposed	1.5027(0.1851)	1.3360(0.1724)	1.0447(0.1167)
Prediction error PSD $\mathbf{S}_e$	Exact	10		
	PX-EM	9.96(0.0979)		
	Proposed	9.83(0.1238)		
	CPU time to calculate the MPVs			
PX-EM	6.28s			
Proposed	0.17s			
	Iteration numbers		NLLF value	
PX-EM	100		4511	
Proposed	7		4509	

The identification results are reported in Table 6. The proposed method provides satisfactory identification of natural frequencies and damping ratios, with errors falling within an acceptable range

when compared to the true values. Although the MAC values for the mode shapes are slightly lower than those for the two closely spaced modes, they still remain within a reasonable range. This indicates that identifying the three closely spaced modes is more challenging.

However, for the PX-EM method, the identification results are less accurate for the last two modes. This is likely due to a significant discrepancy between the initial frequency guesses (1.0376 Hz and 1.0489 Hz) and the true values (1.02 Hz and 1.04 Hz) for these modes, causing the algorithm to converge to a local optimal. This discrepancy is reflected in the results, where the MAC values and modal force identification results are less accurate for the last two modes. The large C.O.V. observed for the MAC in the last two modes (5.0571) compared to the first mode (0.3588) indicates substantial errors exist.

In terms of computation efficiency, the proposed method completes the search of MPVs in 0.25 s, while the PX-EM method takes 1.67 s. The steps required to achieve convergence for both methods are also displayed in Figure 11. Once again, the proposed method has demonstrated its superiority in computation efficiency.

5 Experimental test

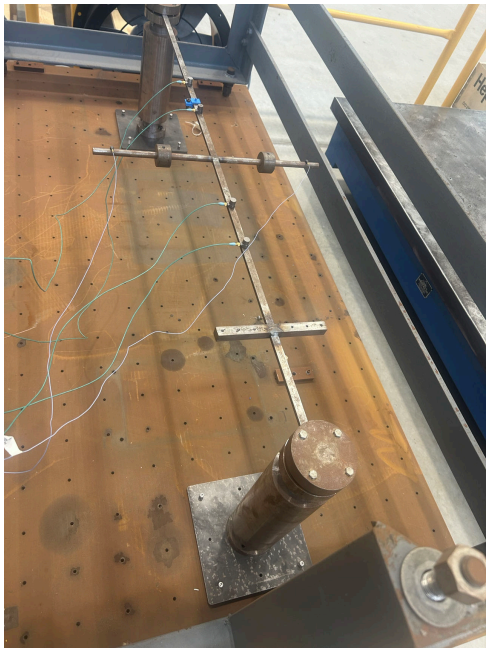

Figure 12: Experimental setting of the clamped-clamped cross beam.

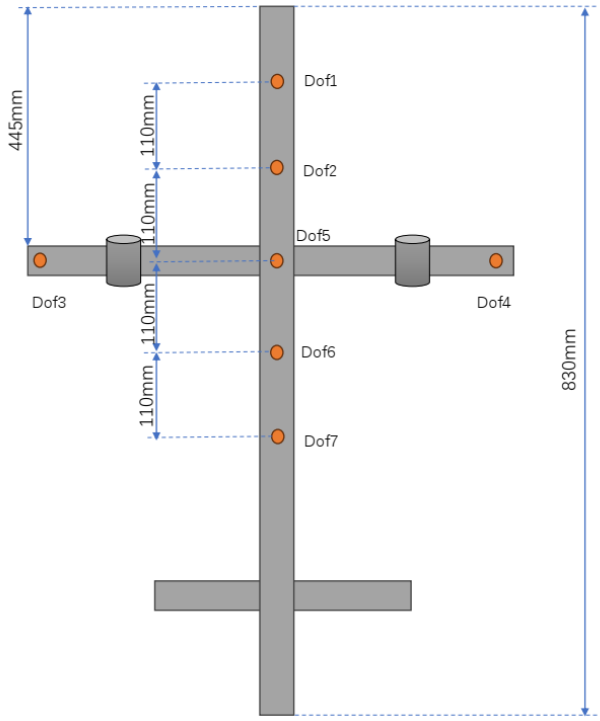

Figure 13: Schematic setting of seven accelerometers (marked as Dof1, Dof2, ..., Dof7) on the beam.

The experimental setup proposed in [39] was implemented and tested in the Swansea Vibration Lab to experimentally assess the performance of the proposed method. The structure is made of two beams that are linked in the middle, as shown in Figure 12. For geometric parameters, the main beam has a length, width, and thickness of 830 mm, 12 mm, and 6 mm, respectively, while the cross-beam has a length of 445 mm and a diameter of 12 mm. The diameter and width of the concentrated masses are 40 mm and 25 mm, respectively. The material properties of the beam are characterized by a Young's modulus of $E = 210\text{GPa}$ and a mass density of $\rho = 7800\text{kg/m}^3$. The main beam is clamped at both ends and attached in the middle to a cross-beam, which has a mass on each side that can be moved. These masses allow the adjustment of the torsional inertia of the system with little impact on the bending inertia. By varying the position of the masses, the desired close frequencies can be easily achieved through mass adjustments. As will be shown later, two close frequencies that match the first bending and torsion modes arise.

Figure 13 illustrates the schematic setting of the accelerometers on the test beam, with specification of the dimensions of the structure and the positions of the accelerometers. The experimental test was conducted using a DP-700A analyser. Impulse hammer excitation was employed as the input loading. Seven accelerometers were strategically placed at reference points to measure the deflection responses, and the impulse hammer was applied at designated points for input. The sampling frequency was set to 2048 Hz, and the test duration was 32 s. Time histories of measured vertical accelerations at all seven positions are presented in Figure 14. Figure 15 shows the singular values of the response PSD using the acceleration data within the frequency interval [0, 300] Hz where the frequency bands for later analysis around the four peaks are selected as [18.5,20.5]Hz, [109.6,111.6]Hz, [155.7,157.7]Hz and [236.5,240.5]Hz, respectively. As can be seen, at the first peak, the first two singular values, at a high level, are much greater than the third one, indicating that there are two close frequencies around this peak. While for other three peaks, the first singular values are much greater than others and therefore, these peaks are associated with well-separated modes. Thus, the study here is mainly focused on the two closely spaced modes around the first peak, for which both the proposed and PX-EM methods are applied. Of course, for other peaks with well-separated modes, the proposed

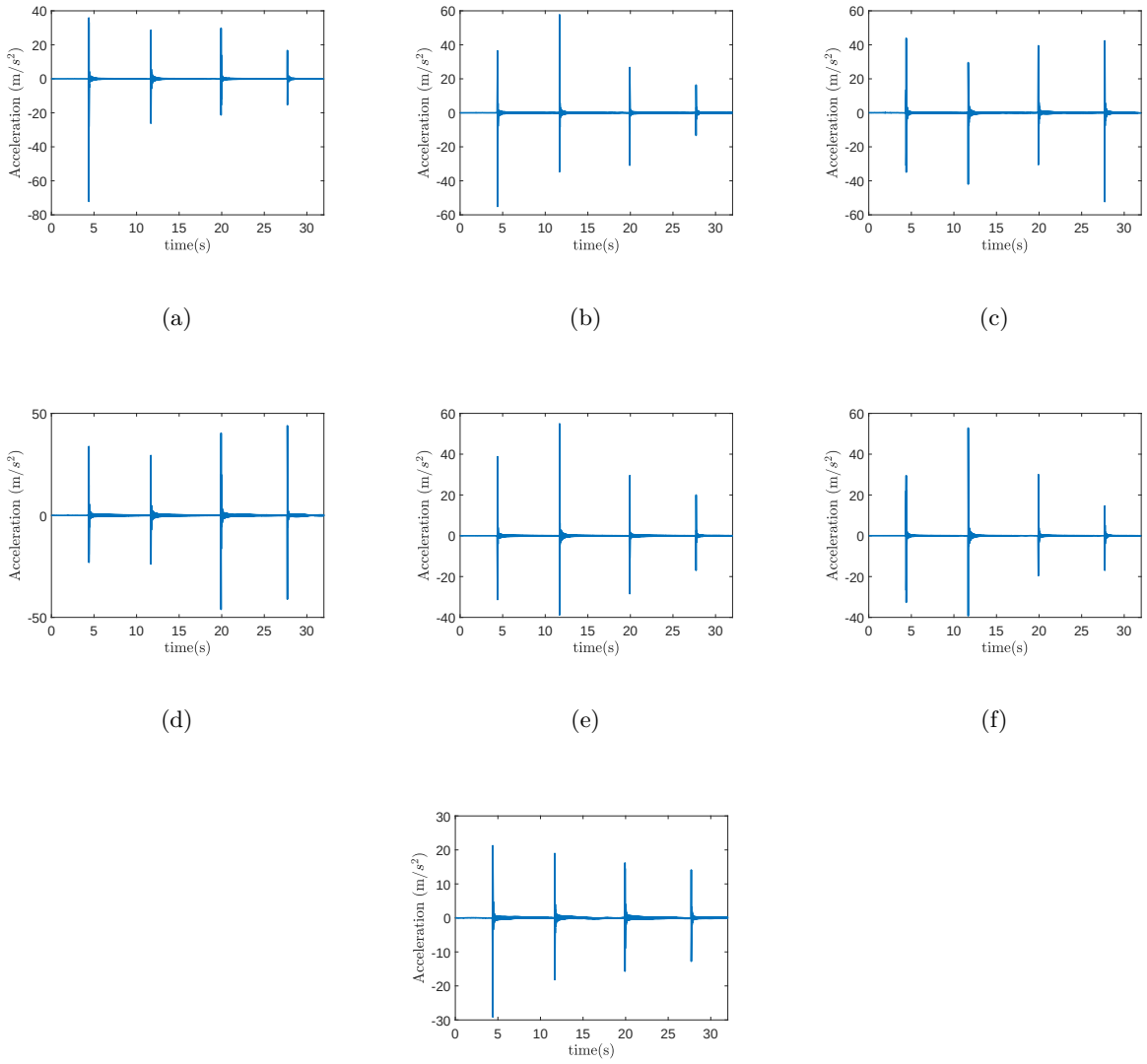

Figure 14: Measured acceleration data of the clamped-clamped cross beam: (a) Dof1, (b) Dof2, (c) Dof3, (d) Dof4, (e) Dof5, (f) Dof6, (g) Dof7.

method is also easily and directly applicable by setting $m = 1$. The only difference is that in the first stage, there is no need to minimize with respect to $\mathbf{R}$ because it is directly set to 1, i.e., $\mathbf{R} = 1$.

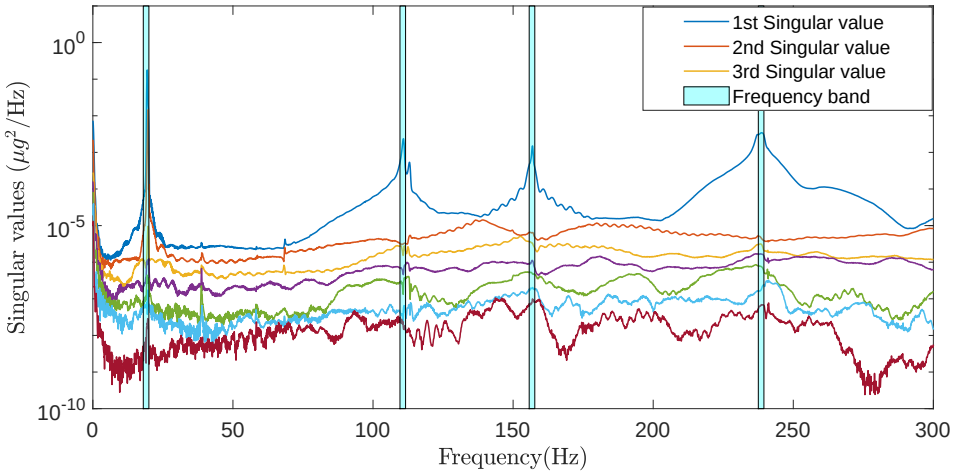

Figure 15: Singular values of response PSD for measured experimental data

Table 7: Modal parameters identification results including the means and the c.o.v (in brackets) at the first peak with two close frequencies of the beam. The CPU time and Iteration numbers to calculate the MPVs as well as the eventual NLLF value is also presented. 'Reference' stands for the results of SSI.

Parameter		Mode 1	Mode 2
Frequency f_i[Hz]	Reference	19.41	19.74
	Initial value	19.41	19.78
	PX-EM	19.41(0.0009)	19.75(0.0012)
	Proposed	19.42(0.0009)	19.78(0.0012)
Damping ratio ζ_i[%]	Reference	0.30	0.43
	Initial value	1	1
	PX-EM	0.26(0.3333)	0.52(0.2494)
	Proposed	0.32(0.3029)	0.49(0.2512)
Mode shape MAC	PX-EM	0.9973(0.0491)	0.9921(0.2204)
	Proposed	0.9978(0.0227)	0.9919(0.1038)
Modal force PSD $\mathbf{S}$	PX-EM	14.99(0.1393)	4.334(0.1524)
	Proposed	8.879(0.0610)	3.540(0.1167)
Prediction error PSD $\mathbf{S}_e$	PX-EM	8.06(0.0599)	
	Proposed	8.05(0.0555)	
	CPU time to calculate the MPVs		
PX-EM	0.45s		
Proposed	0.03s		
	Iteration numbers		NLLF value
PX-EM	24		201.85
Proposed	17		202.62

Table 8: Modal parameters identification results including the means and the c.o.v (in brackets) for the three well-separated modes of the beam. 'Reference' stands for the results of SSI.

Parameter		Mode 3	Mode 4	Mode 5
Frequency f_i[Hz]	Reference	110.83	156.66	238.53
	Proposed	110.62(0.0013)	156.74(0.0004)	238.41(0.0013)
Damping ratio ζ_i[%]	Reference	0.99	0.38	1.00
	Proposed	1.02(0.1745)	0.28(0.2236)	1.02(0.3284)
Mode shape MAC	Proposed	0.9959(0.0091)	0.9939(0.0087)	0.9970(0.0041)

The detailed identification results of the two closely spaced modes around the first peak are tabulated in Table 7, while those of other three well-separated modes are listed in Table 8. Herein, to quantify the accuracy of the identified modal parameters, the well-recognized stochastic subspace identification (SSI) method is adopted to get the reference results for which the stabilization diagram is shown in Figure 16. Then, in the tables, the mode shape MAC is calculated between the identified and reference mode shapes. For schematic view of the identified mode shapes, refer to Figures 17 and 18 for results by the PX-EM and proposed methods, respectively. It can be concluded from the results that

- In Table 7, the comparison of the results on the first two closely spaced modes by the two methods indicates a noteworthy proximity, affirming the accuracy of the proposed method.

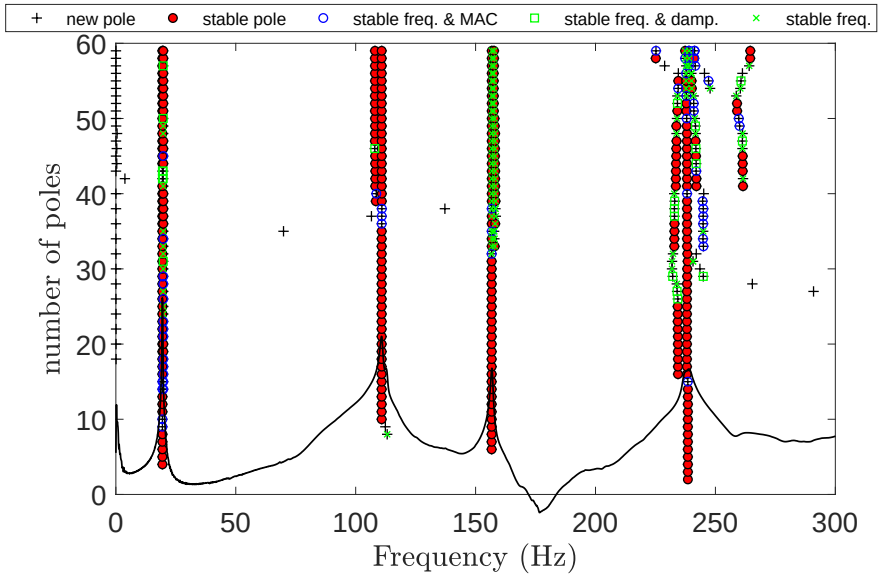

Figure 16: Stabilization diagram for SSI-based modal analysis of measured experimental data

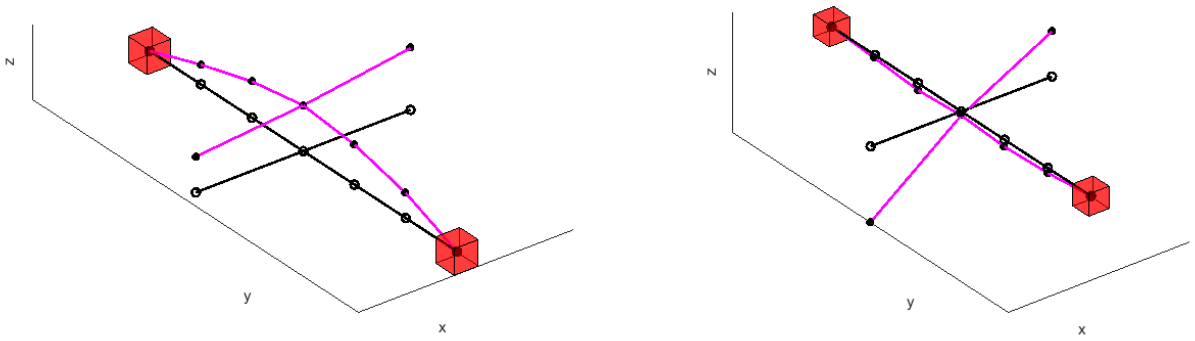

(a) (b)

Figure 17: First two estimated mode shapes by the PX-EM method: (a) f_1=19.41 Hz, (b) f_2=19.75 Hz

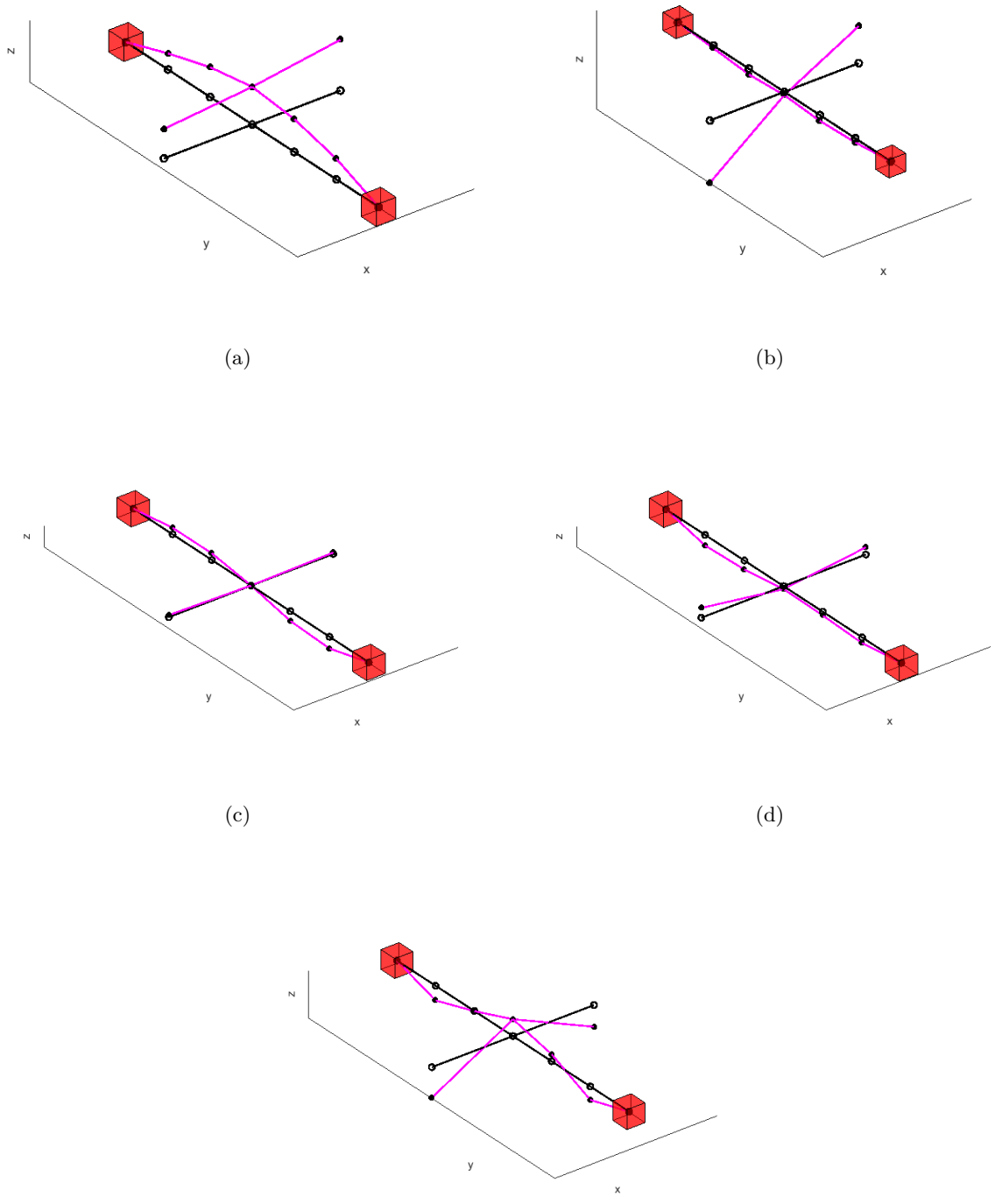

(a) (b)

(c) (d)

(e)

Figure 18: First five estimated mode shapes by the proposed method: (a) $f_1 = 19.42$ Hz, (b) $f_2 = 19.78$ Hz, (c) $f_3 = 110.62$ Hz, (d) $f_4 = 156.74$ Hz, (e) $f_5 = 238.52$ Hz.

The expected MAC values closely approach 1, signifying a similarly good identification of the two closely spaced mode shapes between the two methods. Computational simulations were conducted using MATLAB 2020a on an Intel(R) Core(TM) i9-7920X computer and the CPU time to calculate the MPVs is also determined. Again, the proposed method takes much less time than the PX-EM method, demonstrating its practical efficiency for on-site applications.

- Analysis of the c.o.v, which measures the relative dispersion of the data, reveals that damping ratios are identified with considerably higher uncertainty compared to natural frequencies. Damping ratios exhibit a c.o.v in the order of a few tens of percent. In contrast, natural frequencies demonstrate a c.o.v of only 0.1%. This result is consistent with practical experience, as identifying damping ratios is usually more challenging than identifying natural frequencies. The natural frequency estimation is very accurate, as indicated by the small posterior c.o.v. The posterior uncertainties related to damping ratios are much higher than those of natural frequencies, suggesting that damping ratios are harder to identify exactly.

- The proposed method can be directly extended to identify well-separated modes. By Table 8, the identification results are rather satisfactory, in comparison to the referenced SSI results, because the difference in natural frequencies is always less than 0.21 Hz, while the MAC of all mode shapes exceeds 0.99.

6 Field test

To evaluate the proposed method under more challenging conditions, the Canton Tower [40], a benchmark structure for SHM in tall buildings, was selected as a case study. The Canton Tower serves as a platform for comparing the performance of various SHM methods. Several approaches have been applied to identify the modal parameters of the Canton Tower in previous studies, including the SSI method [41], the Bayesian spectral density approach [42], and the Bayesian FFT method [43, 30]. In this study, the identified modal parameters are compared with the results obtained from the SSI and PX-EM methods.

To capture the dynamic response of the Canton Tower, twenty uni-axial accelerometers were strategically installed at various locations along the tower's height. Continuous 24-hour field measurements of structural acceleration time histories were recorded, along with ambient conditions such as temperature and wind properties. Comprehensive details of the SHM system's modular design, the benchmark problem's task requirements, and the finite element models are available in the referenced studies [44].

The field test was conducted under ambient excitation conditions, with a sampling frequency of 50 Hz. Figure 19 illustrates three time series recorded at 07:00 on February 20, 2010, spanning a total duration of 20 minutes.

Figure 20 illustrates the singular values of the response PSD derived from the acceleration data within the frequency range of [0, 1.5] Hz. This range encompasses one three-mode band, one two-mode band, and seven single-mode bands. For further analysis, seven single frequency bands corresponding to well-separated mode peaks were selected: [0.08, 0.10] Hz, [0.12, 0.15] Hz, [0.34, 0.39] Hz, [0.40, 0.43] Hz, [0.72, 0.83] Hz, [0.91, 1.00] Hz, and [1.22, 1.27] Hz.

Within the [0.44, 0.55] Hz band, the first three singular values are significantly higher than the remaining ones, indicating the presence of three closely spaced frequencies. Similarly, the [1.12, 1.21] Hz band reveals two closely spaced modes. The study focuses on these closely spaced modes, applying both the proposed method and the PX-EM method for detailed analysis.

The detailed identification results for the closely spaced modes are summarized in Table 9. The SSI method serves as the reference, with its stabilization diagram depicted in Figure 21. The mode shape MAC values between the identified modes and the SSI reference modes are also calculated.

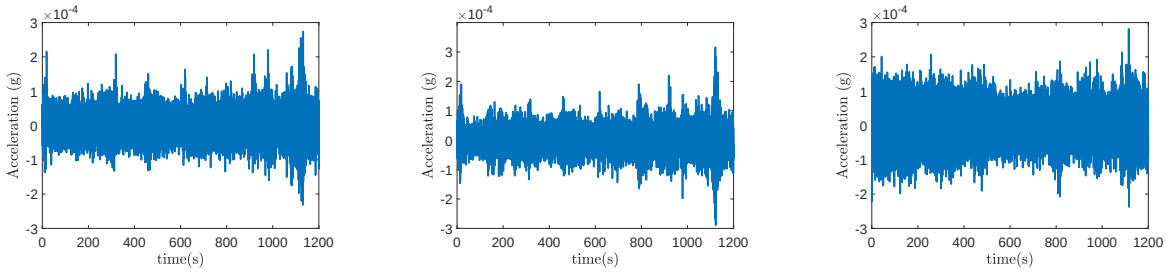

(a) (b) (c)

Figure 19: Measured acceleration data of field test: (a) Dof1, (b) Dof2, (c) Dof3.

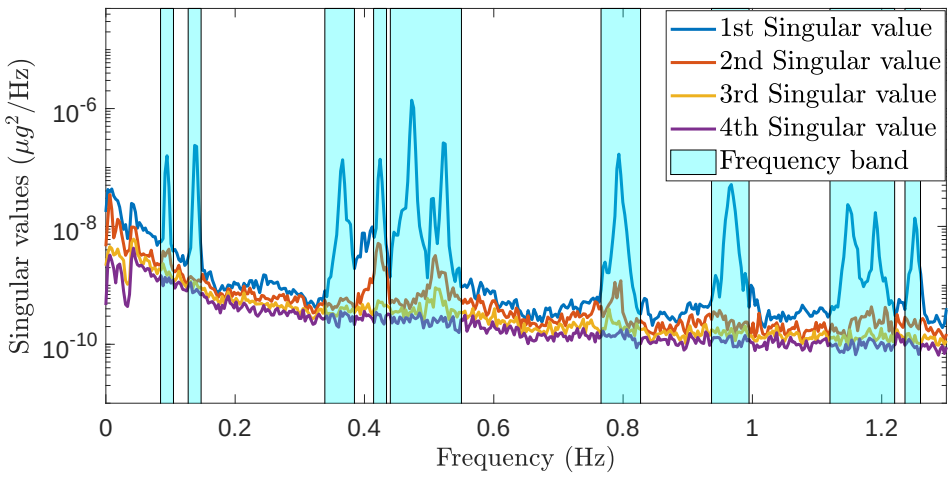

Figure 20: Singular values of the 20 channels acceleration measurements (from 7:00 to 7:20 on 20th January, 2010)

Figures 23 and 22 illustrate the identified mode shapes along the X-axis and Y-axis directions for both the PX-EM and proposed methods. Notably, Mode 6 and Mode 12 exhibit significant torsional behavior. Key observations and comparisons are outlined below:

- **Closely Spaced Modes**: The comparison of closely spaced modes identified by both methods demonstrates excellent agreement, further validating the accuracy of the proposed method. The MAC values exceed 0.989, indicating a high level of similarity in the identified mode shapes. Moreover, the computational time and iteration counts required for MPV calculations underscore the efficiency of the proposed method. Remarkably, the proposed method significantly outperforms the PX-EM method in terms of computation time, reinforcing its practical suitability for on-site applications.
- **Well-Separated Modes (Table 9)**: The identification results for the well-separated modes are highly consistent with the reference SSI results. Natural frequency differences are always less than 0.01 Hz, and all mode shape MAC values exceed 0.98, underscoring the accuracy of the proposed method.
- **Frequencies and Damping Ratios**: The coefficients of variation (COVs) for modal frequencies are quite small (less than 0.2%), indicating high accuracy in the MPVs. The identified damping ratios for this structure are also very small, with all modes below 1%, aligning with the results by Li et al. [30] for the same structure under ambient vibration conditions. However, the posterior uncertainty of damping ratios is relatively high compared to modal frequencies, often in the range of tens of percent. This highlights the inherent difficulty of accurately identifying damping ratios.
- **PSD and Prediction Error**: The PSD of modal force and PSD of prediction error are strongly influenced by the excitation environment. Notably, the decreasing trend in the MPV of prediction error PSD observed in Table 9 which corresponds well with the SV spectrum shown in Figure 20.
- **Mode Shapes**: In terms of COVs for mode shapes, rotational modes exhibit relatively larger posterior COVs, emphasizing the challenges in identifying torsional mode shapes accurately.

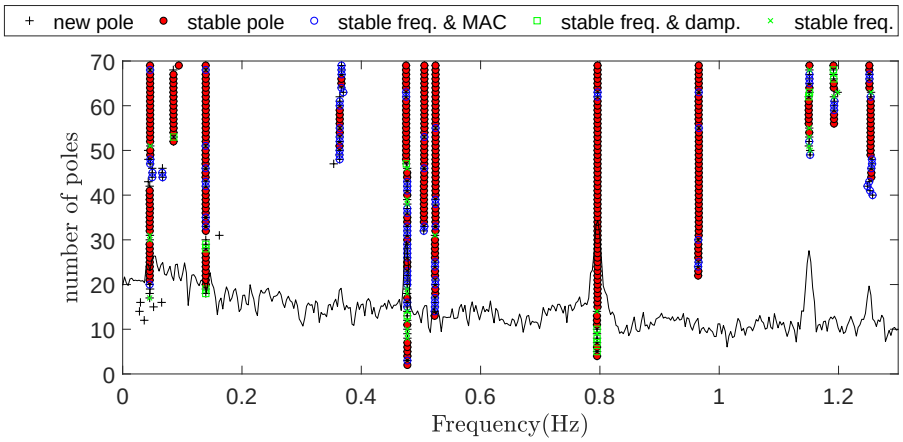

Figure 21: Stabilization diagram for SSI-based modal analysis of measured field data

Table 9: Modal parameters identification results including the means and the c.o.v (in brackets) for the Canton tower. 'Reference' stands for the results of SSI.

Mode	Parameter	Reference	Proposed	PX-EM
Mode 1	Frequency f_i[Hz]	0.0941	0.0942 (0.0016)	0.0934(0.0039)
	Damping ratio ζ_i[%]	1.07	0.49 (0.7258)	0.88(0.4645)
	Mode shape MAC		0.9914(0.0390)	0.9900(0.0812)
	Modal force PSD S $[(\mu g)^2/Hz]$		56.3 (0.2026)	54.6(0.2627)
	Prediction error PSD S_e $[(\mu g)^2/Hz]$		358.1 (0.0377)	355.9(0.0459)
Mode 2	Frequency f_i[Hz]	0.1363	0.1391 (0.0014)	0.1387(0.0017)
	Damping ratio ζ_i[%]	2.74	0.48 (0.4771)	0.32(0.6956)
	Mode shape MAC		0.9959 (0.0276)	0.9952(0.0314)
	Modal force PSD S $[(\mu g)^2/Hz]$		43.08 (0.1849)	56.73(0.2266)
	Prediction error PSD S_e $[(\mu g)^2/Hz]$		224.93 (0.0377)	220.22(0.0459)
Mode 3	Frequency f_i[Hz]	0.3654	0.3657 (0.0010)	0.3660(0.0012)
	Damping ratio ζ_i[%]	0.43	0.37 (0.2926)	0.33(0.4002)
	Mode shape MAC		0.9974 (0.0253)	0.9986(0.0312)
	Modal force PSD S $[(\mu g)^2/Hz]$		6.68 (0.1221)	8.34(0.2446)
	Prediction error PSD S_e $[(\mu g)^2/Hz]$		78.02 (0.0240)	81.86(0.0294)
Mode 4	Frequency f_i[Hz]	0.4240	0.4245 (0.0011)	0.4233(0.0014)
	Damping ratio ζ_i[%]	0.25	0.26 (0.2918)	0.41(0.3513)
	Mode shape MAC		0.9939 (0.0571)	0.9908 (0.0758)
	Modal force PSD S $[(\mu g)^2/Hz]$		2.28 (0.2065)	1.96(0.2472)
	Prediction error PSD S_e $[(\mu g)^2/Hz]$		102.7 (0.0309)	100.17(0.0377)
Mode 5	Frequency f_i[Hz]	0.4746	0.4758 (0.0005)	0.4746(0.0003)
	Damping ratio ζ_i[%]	0.13	0.11 (0.4728)	0.07(0.5651)
	Mode shape MAC		0.9999 (0.090)	0.9952(0.0452)
	Modal force PSD S $[(\mu g)^2/Hz]$		27.17 (0.0901)	20.22(0.0754)
	Prediction error PSD S_e $[(\mu g)^2/Hz]$		64.40 (0.0212)	61.54(0.0172)
Mode 6	Frequency f_i[Hz]	0.5052	0.5073 (0.0009)	0.5055(0.0005)
	Damping ratio ζ_i[%]	0.07	0.27 (0.3725)	0.16 (0.3451)
	Mode shape MAC		0.9952 (0.0452)	0.9932 (0.0306)
	Modal force PSD S $[(\mu g)^2/Hz]$		8.39 (0.1896)	5.40(0.0873)
	Prediction error PSD S_e $[(\mu g)^2/Hz]$		64.40 (0.0212)	61.54(0.0172)
Mode 7	Frequency f_i[Hz]	0.5222	0.5231 (0.0007)	0.5225(0.0005)
	Damping ratio ζ_i[%]	0.13	0.21 (0.3844)	0.18(0.3228)
	Mode shape MAC		0.9989 (0.0292)	0.9988(0.0212)
	Modal force PSD S $[(\mu g)^2/Hz]$		10.94 (0.1486)	8.72(0.0873)
	Prediction error PSD S_e $[(\mu g)^2/Hz]$		64.40 (0.0212)	61.54(0.0172)
Mode 8	Frequency f_i[Hz]	0.7943	0.7945 (0.0005)	0.7956(0.0006)
	Damping ratio ζ_i[%]	0.23	0.22 (0.2140)	0.25(0.2759)
	Mode shape MAC		1 (0.0088)	0.9995(0.0099)
	Modal force PSD S $[(\mu g)^2/Hz]$		21.71 (0.0810)	20.23(0.0964)
	Prediction error PSD S_e $[(\mu g)^2/Hz]$		68.72 (0.0163)	60.82(0.0199)
Mode 9	Frequency f_i[Hz]	0.9642	0.9650 (0.0005)	0.9654(0.0006)
	Damping ratio ζ_i[%]	0.27	0.29 (0.1976)	0.26(0.2517)
	Mode shape MAC		0.997 (0.0145)	0.9990(0.157)
	Modal force PSD S $[(\mu g)^2/Hz]$		4.62 (0.0831)	4.98(0.1085)
	Prediction error PSD S_e $[(\mu g)^2/Hz]$		50.51 (0.0180)	43.05(0.0220)
Mode 10	Frequency f_i[Hz]	1.1491	1.1520 (0.0004)	1.1510(0.0004)
	Damping ratio ζ_i[%]	0.08	0.15 (0.3061)	0.14(0.3112)
	Mode shape MAC		0.9996 (0.0258)	0.9996 (0.0252)
	Modal force PSD S $[(\mu g)^2/Hz]$		0.77(0.1168)	0.84(0.1344)
	Prediction error PSD S_e $[(\mu g)^2/Hz]$		32.39 (0.0224)	34.22(0.0231)
Mode 11	Frequency f_i[Hz]	1.1895	1.1926 (0.0004)	1.1919(0.0003)
	Damping ratio ζ_i[%]	0.11	0.13 (0.3272)	0.12(0.3140)
	Mode shape MAC		0.9882 (0.0317)	0.9895(0.0320)
	Modal force PSD S $[(\mu g)^2/Hz]$		0.43 (0.1197)	0.49(0.1562)
	Prediction error PSD S_e $[(\mu g)^2/Hz]$		32.39 (0.0224)	34.22(0.0231)
Mode 12	Frequency f_i[Hz]	1.2484	1.2521 (0.0003)	1.2517(0.0003)
	Damping ratio ζ_i[%]	0.13	0.13 (0.2629)	0.10(0.3487)
	Mode shape MAC		0.9977 (0.0215)	0.9980(0.0232)
	Modal force PSD S $[(\mu g)^2/Hz]$		0.71 (0.1226)	0.70(0.1467)
	Prediction error PSD S_e $[(\mu g)^2/Hz]$		46.17 (0.0240)	43.50(0.0294)

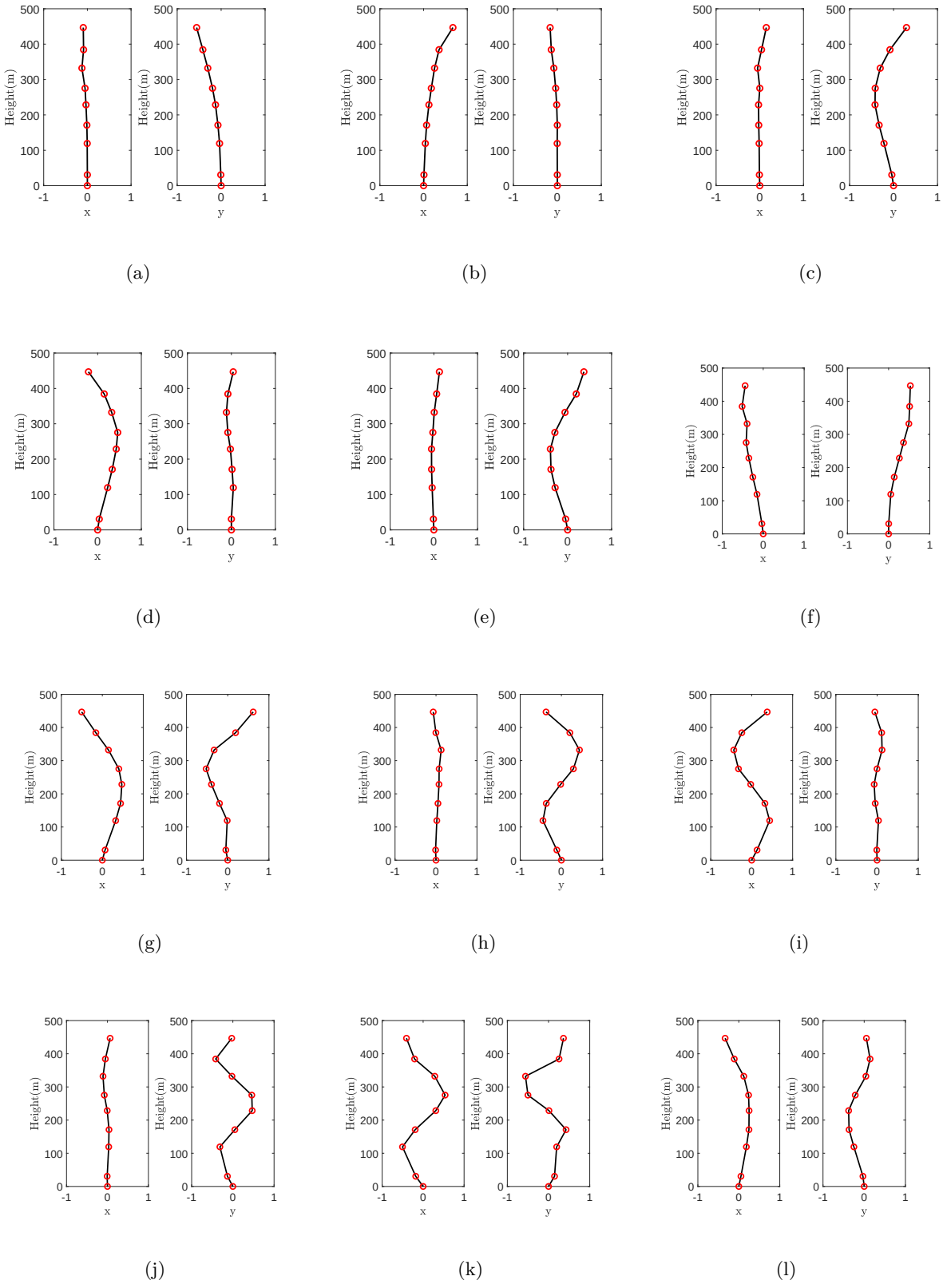

Figure 22: Estimated mode shapes by the proposed method: (a) Mode 1, (b) Mode 2, (c) Mode 3, (d) Mode 4, (e) Mode 5, (f) Mode 6, (g) Mode 7, (h) Mode 8, (i) Mode 9, (j) Mode 10, (k) Mode 11, (l) Mode 12.

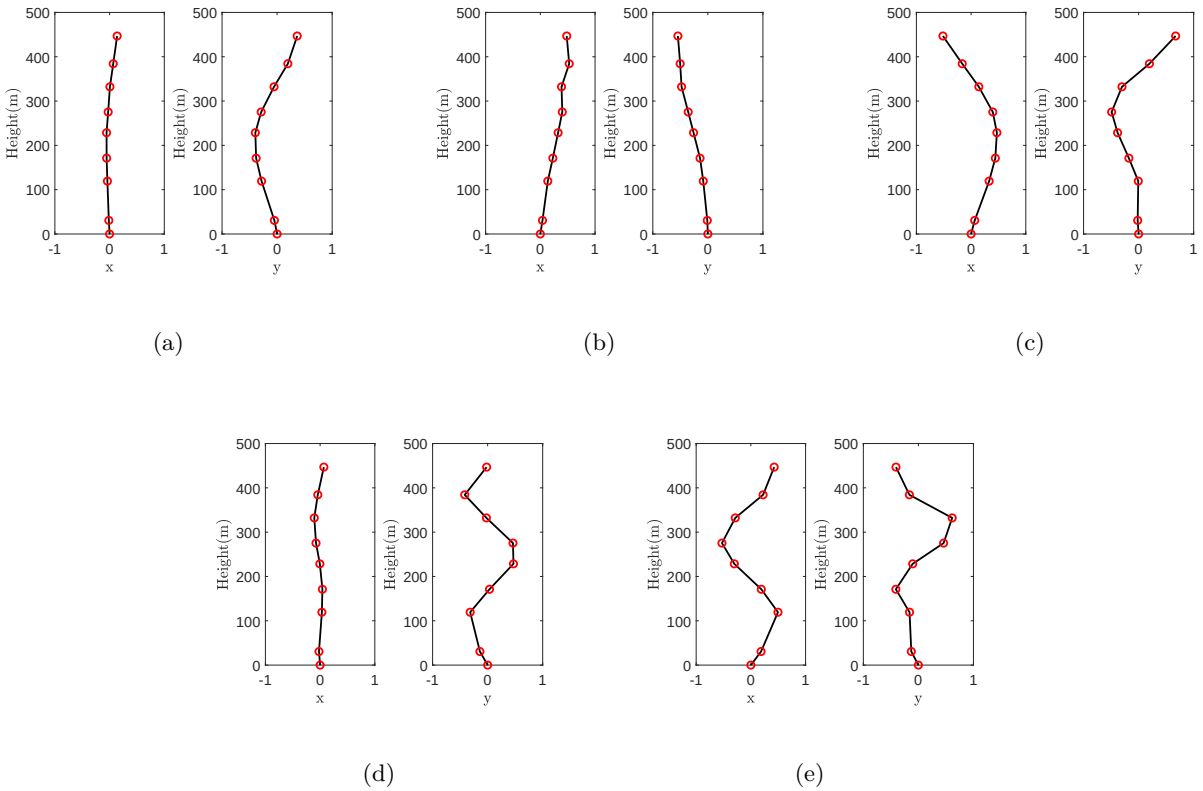

Figure 23: Estimated closely spaced mode shapes by the PX-EM method: (a) Mode 5, (b) Mode 6, (c) Mode 7, (d) Mode 10, (e) Mode 11.

7 Conclusion

A two-stage method has been proposed to robustly and efficiently address the challenges associated with closely spaced modes in Bayesian FFT-based modal analysis. The key lies in reformulating the mode shape identification into the JAD problem, circumventing the challenging problem in providing a good initial guess of closely spaced mode shapes, and then, the Bayesian FFT optimization procedure is decoupled into two sequential stages, leading to a substantial improvement of computation efficiency. Two numerical examples and an experimental case are studied, yielding the following key findings:

- The proposed method gives more accurate identification of closely spaced mode shapes with the MAC closer to 1 than the PX-EM method, especially when the initial guess of frequency is inaccurately selected (e.g., in the first numerical example) and when there are more than two closely spaced modes (e.g., in the second numerical example). This also indicates that reformulation of mode shape identification in Bayesian FFT to the JAD problem is robust and well-posed. Moreover, since there is no need to specify an initial guess for solving the JAD problem, this reformulation subtly circumvents the challenging problem in providing a good initial guess for Bayesian FFT so as to avoid convergence to undesired local optima.
- The proposed method exhibits remarkable efficiency in computational time. The efficiency stands in contrast to the PX-EM method, which takes much more time to calculate the MPVs, especially for the case with more than two closely spaced modes (e.g., in the second numerical example). The improvement in efficiency is mainly attributed to the decoupling property of the proposed method in two stages and yet, the independent iteration procedure for different modes in the second stage.

Acknowledgment

The PX-EM code used in this paper, as proposed in [30], was provided by Dr. Li and the authors would like to express the sincere gratitude for his valuable help and contribution. Financial supports from National Natural Science Foundation of China (No. 12472060), the Key-Area Research and Development Program of Guangdong Province (No. 2022B0101080001) and Guangdong Basic and Applied Basic Research Foundation (No. 2023A1515240046) are gratefully acknowledged.

Data Availability

Data available on request from the authors.

Compliance with ethical standards

Conflict of interest

The authors declare that they have no conflict of interest.

Appendix A

On the approximate diagonality of the modal response PSD $\mathbf{H}_k$

The approximate diagonality of the modal response PSD $\mathbf{H}_k$ or mutually uncorrelation of different modal responses plays a key role in the derivation of the proposed approach. Such a property has been frequently used in the modal analysis through blind source separation [2, 36, 37] or frequency

domain decomposition [12, 34]. Herein, this property is specifically derived in both frequency and time domains. To do so, the relationship between the uncontaminated structural response PSD $\mathbf{E}(\omega)$ and the external force PSD $\mathbf{S}_p(\omega)$ can be established as [12],

$$\mathbf{E}(\omega) = \mathbf{G}(\mathrm{i}\omega)\mathbf{S}_p(\omega)\mathbf{G}^H(\mathrm{i}\omega) \tag{A.1}$$

where the superscript H denotes the conjugate transpose operator, $\mathbf{G}(\mathrm{i}\omega)$ is the frequency response function (FRF) matrix [34], defined as

$$\mathbf{G}(\mathrm{i}\omega) = [(\mathrm{i}\omega)^2\mathbf{M}_s + (\mathrm{i}\omega)\mathbf{C}_s + \mathbf{K}_s]^{-1} = \sum_{k=1}^{n}[\frac{\mathbf{O}_k}{\mathrm{i}\omega - \lambda_k} + \frac{\mathbf{O}_k^*}{\mathrm{i}\omega - \lambda_k^*}], \tag{A.2}$$

$\mathbf{M}_s, \mathbf{C}_s, \mathbf{K}_s$ are the mass, damping and stiffness matrices, λ_k, λ_k^* are the poles and the superscript * means the conjugate operator. When the damping is proportional, there are

$$\lambda_k = -\zeta_k\omega_k + \mathrm{i}\omega_{dk} = -\zeta_k\omega_k + \mathrm{i}\omega_k\sqrt{1-\zeta_k^2} \tag{A.3}$$

and

$$\mathbf{O}_k = u_k\phi_k\phi_k^T \tag{A.4}$$

where $\mathbf{O}_k$ is the kth residue matrix and u_k is a complex constant, known as the modal participation factor.

For simplicity, assume that ω_k, ω_{k+1} are two close frequencies and are well separated from others. Let ω be around the peaks of the two close frequencies, designated as $\omega \in \mathrm{sub}(\omega_k, \omega_{k+1})$, and then, $\mathbf{S}_p(\omega) = \mathbf{S}_p$ is reasonably assumed to be constant. Considering this, substitution of Eq. (A.2) into Eq. (A.1) yields

$$\mathbf{E}(\omega) = \sum_{k=1}^{n}\sum_{s=1}^{n}[\frac{\mathbf{O}_k}{\mathrm{i}\omega - \lambda_k} + \frac{\mathbf{O}_k^*}{\mathrm{i}\omega - \lambda_k^*}]\mathbf{S}_p[\frac{\mathbf{O}_s}{\mathrm{i}\omega - \lambda_s} + \frac{\mathbf{O}_s^*}{\mathrm{i}\omega - \lambda_s^*}]^H. \tag{A.5}$$

By applying the Heaviside partial-fraction expansion theorem, Eq. (A.5) can become

$$\mathbf{E}(\omega) = \sum_{k=1}^{n}\frac{\mathbf{B}_k}{\mathrm{i}\omega - \lambda_k} + \frac{\mathbf{B}_k^*}{\mathrm{i}\omega - \lambda_k^*} + \frac{\mathbf{B}_k^T}{-\mathrm{i}\omega - \lambda_k} + \frac{\mathbf{B}_k^H}{-\mathrm{i}\omega - \lambda_k^*} \tag{A.6}$$

where

$$\mathbf{B}_k = \mathbf{O}_k\mathbf{S}_p\sum_{s=1}^{n}(\frac{\mathbf{O}_s^T}{-\lambda_k - \lambda_s} + \frac{\mathbf{O}_s^H}{-\lambda_k - \lambda_s^*}). \tag{A.7}$$

Assuming light damping $\zeta_k, \zeta_{k+1} \to 0$, it is easily deduced for $\omega \in \mathrm{sub}(\omega_k, \omega_{k+1})$ that

$$\{|\mathrm{i}\omega - \lambda_k|, |\mathrm{i}\omega - \lambda_{k+1}|, |-\mathrm{i}\omega - \lambda_k^*|, |-\mathrm{i}\omega - \lambda_{k+1}^*|\} \ll \begin{cases} \{|\mathrm{i}\omega - \lambda_s|, |-\mathrm{i}\omega - \lambda_s^*|, s \neq k, k+1\}, \\ \{|\mathrm{i}\omega - \lambda_s^*|, |-\mathrm{i}\omega - \lambda_s|, \forall s\}. \end{cases} \tag{A.8}$$

This indicates that the kth and $k+1$th modes contribute most to $\mathbf{E}(\omega)$ in (A.6) and other terms can be ignored, leading to

$$\mathbf{E}(\omega) \approx \frac{\mathbf{B}_k}{\mathrm{i}\omega - \lambda_k} + \frac{\mathbf{B}_k^H}{-\mathrm{i}\omega - \lambda_k^*} + \frac{\mathbf{B}_{k+1}}{\mathrm{i}\omega - \lambda_{k+1}} + \frac{\mathbf{B}_{k+1}^H}{-\mathrm{i}\omega - \lambda_{k+1}^*} = 2\mathrm{Re}\frac{\mathbf{B}_k}{\mathrm{i}\omega - \lambda_k} + 2\mathrm{Re}\frac{\mathbf{B}_{k+1}}{\mathrm{i}\omega - \lambda_{k+1}}. \tag{A.9}$$

Again, considering the light damping, it is analogously found that

$$\begin{aligned} &-\lambda_k - \lambda_k^* = 2\zeta_k\omega_k, -\lambda_k - \lambda_{k+1}^* = (\zeta_k\omega_k + \zeta_{k+1}\omega_{k+1}) + \mathrm{i}(\omega_{d(k+1)} - \omega_{dk}) \\ &\Rightarrow \{|-\lambda_k - \lambda_k^*|, |-\lambda_k - \lambda_{k+1}^*|\} \ll \begin{cases} \{|-\lambda_k - \lambda_s^*|, s \neq k, k+1\}, \\ \{|-\lambda_k - \lambda_s|, \forall s\}. \end{cases} \end{aligned} \tag{A.10}$$

and then, $\mathbf{B}_k$ in Eq. (A.7) can be approximated as [34]

$$\begin{aligned}\mathbf{B}_k &\approx \mathbf{O}_k\mathbf{S}_p \sum_{s=k,k+1} \frac{\mathbf{O}_s^H}{-\lambda_k - \lambda_s^*} \\ &= \frac{\mathbf{O}_k\mathbf{S}_p\mathbf{O}_k^H}{2\zeta_k\omega_k} + \frac{\mathbf{O}_k\mathbf{S}\mathbf{O}_{k+1}^H}{(\zeta_k\omega_k+\zeta_{k+1}\omega_{k+1})+\mathrm{i}(\omega_{d(k+1)}-\omega_{dk})} \\ &= \gamma_k\phi_k\phi_k^T + \alpha_k\phi_k\phi_{k+1}^T\end{aligned} \tag{A.11}$$

with $\gamma_k = \frac{|u_k|^2\phi_k^T\mathbf{S}_p\phi_k}{2\zeta_k\omega_k}$ and $\alpha_k = \frac{u_k u_{k+1}^*\phi_k^T\mathbf{S}_p\phi_{k+1}}{(\zeta_k\omega_k+\zeta_{k+1}\omega_{k+1})+\mathrm{i}(\omega_{d(k+1)}-\omega_{dk})}$. Given the approximate orthogonality of the modal vectors, α_k is approximately zero or $|\alpha_k| \ll |\gamma_k|$, allowing to omit the second term in Eq. (A.11). This along with Eq. (A.9) gives rise to

$$\mathbf{E}(\omega) = [\phi_k, \phi_{k+1}] \begin{bmatrix} 2\mathrm{Re}(\frac{\gamma_k}{\mathrm{i}\omega-\lambda_k}) & 0 \\ 0 & 2\mathrm{Re}(\frac{\gamma_{k+1}}{\mathrm{i}\omega-\lambda_{k+1}}) \end{bmatrix} [\phi_k, \phi_{k+1}]^T \tag{A.12}$$

By comparing Eq. (A.12) with Eq. (5), the modal response PSD $\mathbf{H}_k$ can be effectively approximated by the real diagonal matrix $\begin{bmatrix} 2\mathrm{Re}(\frac{\gamma_k}{\mathrm{i}\omega-\lambda_k}) & 0 \\ 0 & 2\mathrm{Re}(\frac{\gamma_{k+1}}{\mathrm{i}\omega-\lambda_{k+1}}) \end{bmatrix}$. The above derivations of the approximate diagonality of the modal response PSD $\mathbf{H}_k$ are based on the assumption of two close frequencies, nevertheless, it is straightforward to extend them to the case with three or more close frequencies.

Next, some simple illustrations from the time domain are also presented. Let $q_i(t)$ and $\eta_i(\omega)$ be the respective time- and frequency-domain modal response of the ith mode, i.e., $\eta_i(\omega)$ is the Fourier transform of $q_i(t)$. The approximate diagonality of the modal response PSD indicates that the off-diagonals are far less than diagonals, that is, $|S_{\eta_k\eta_{k+1}}(\omega)| \ll |S_{\eta_k\eta_k}(\omega)|, |S_{\eta_{k+1}\eta_{k+1}}(\omega)|$ for $\omega \in \mathrm{sub}(\omega_k, \omega_{k+1})$ with $S_{\eta_k\eta_{k+1}}(\omega) = \mathbb{E}[\eta_k(\omega)\eta_{k+1}^*(\omega)]$ denoting the cross PSD between η_k and η_{k+1}. Since $\frac{1}{2\pi}\int_0^\infty \eta_i(\omega)\eta_j^*(\omega)\mathrm{d}\omega = \int_0^T q_i(t)q_j(t)\mathrm{d}t$ with T the time duration of the signal, verifying the approximate diagonality of the modal response PSD is to some extent equivalent to show the mutually uncorrelation between $q_k(t), q_{k+1}(t)$, i.e.,

$$|\int_0^T q_k(t)q_{k+1}(t)\mathrm{d}t| \ll \{\int_0^T q_k^2(t)\mathrm{d}t, \int_0^T q_{k+1}^2(t)\mathrm{d}t\} \tag{A.13}$$

which is illustrated in below for light damping $\xi_k, \xi_{k+1} \to 0$ and two close frequencies ω_k, ω_{k+1} through examples,

- In case of free vibration, one can set $q_k(t) = \cos(\omega_k t+\theta_k), q_{k+1}(t) = \cos(\omega_{k+1}t+\theta_{k+1})$ for instance. Then, $\int_0^T q_k^2(t)\mathrm{d}t = \frac{T}{2}+\frac{\sin(2\omega_k T+2\theta_k)-\sin(2\theta_k)}{4\omega_k}$, $\int_0^T q_{k+1}^2(t)\mathrm{d}t = \frac{T}{2}+\frac{\sin(2\omega_{k+1}T+2\theta_{k+1})-\sin(2\theta_{k+1})}{4\omega_{k+1}}$, while $\int_0^T q_k(t)q_{k+1}(t)\mathrm{d}t = \frac{\sin((\omega_{k+1}+\omega_k)T+\theta_{k+1}+\theta_k)-\sin(\theta_{k+1}+\theta_k)}{2(\omega_{k+1}+\omega_k)}+\frac{\sin((\omega_{k+1}-\omega_k)T+\theta_{k+1}-\theta_k)-\sin(\theta_{k+1}-\theta_k)}{2(\omega_{k+1}-\omega_k)}$, which clearly satisfies Eq. (A.13) for large T.

- In case of random vibration, $q_k(t), q_{k+1}(t)$ would be narrow banded signals. In this way, set $q_k(t) = a_k(t)\cos(\omega_k t), q_{k+1}(t) = a_{k+1}(t)\cos(\omega_{k+1}t)$ for instance with $a_k(t), a_{k+1}(t)$ varies very slowly. For simplicity, let $a_k(t) = a_{k+1}(t) = a + b\cos(\omega_s t)$ with $\omega_s/\omega_k, \omega_s/\omega_{k+1} \ll 1, \omega_s \neq \omega_{k+1}-\omega_k$. Then, $\int_0^T q_k^2(t)\mathrm{d}t = a^2T/2 + b^2T/4 + c_k$, $\int_0^T q_{k+1}^2(t)\mathrm{d}t = a^2T/2 + b^2T/4 + c_{k+1}$ with c_{k+1}, c_k bounded constants, while $\int_0^T q_k(t)q_{k+1}(t)\mathrm{d}t$ is bounded for arbitrarily large T. This again verifies Eq. (A.13).

Actually, the mutually uncorrelation between two different modal responses have been widely used in the OMA via blind source separation [2, 36, 37].

Appendix B

Lemma A.1. *For any matrices* $\mathbf{A}$, $\mathbf{B}$, $\mathbf{C}$, $\mathbf{D}$ *of appropriate sizes, with* $\mathbf{A}$, $\mathbf{C}$ *invertible, the following identities hold*

$$(\mathbf{BCD}+\mathbf{A})^{-1}=\mathbf{A}^{-1}-\mathbf{A}^{-1}\mathbf{B}(\mathbf{DA}^{-1}\mathbf{B}+\mathbf{C}^{-1})^{-1}\mathbf{DA}^{-1}, \tag{A.14}$$

and

$$|\mathbf{BCD}+\mathbf{A}|=|\mathbf{A}||\mathbf{C}||\mathbf{DA}^{-1}\mathbf{B}+\mathbf{C}^{-1}|. \tag{A.15}$$

Computation of posterior covariance

To compute the posterior covariance, the NLLF in Eq. (8) should be further analyzed. To begin with, the log-determinant and inversion of the key matrix $\mathbf{E}_k=\bar{\mathbf{\Phi}}\mathbf{H}_k\bar{\mathbf{\Phi}}^T+S_e\mathbf{I}_n$ (with $\bar{\mathbf{\Phi}}=[\phi_1/||\phi_1||,\phi_2/||\phi_2||,\ldots,\phi_m/||\phi_m||]$) are computed by resorting to Lemma A.1,

$$\begin{aligned}
&|\mathbf{E}_k|=S_e^{n-m}|\mathbf{H}_k||\mathbf{P}_k| \quad ,\\
&\mathbf{E}_k^{-1}=S_e^{-1}\mathbf{I}_n-S_e^{-1}\bar{\mathbf{\Phi}}\mathbf{P}_k^{-1}\bar{\mathbf{\Phi}}^T,\\
&\mathbf{P}_k=\bar{\mathbf{\Phi}}^T\bar{\mathbf{\Phi}}+S_e\mathbf{H}_k^{-1}.
\end{aligned} \tag{A.16}$$

Then, the NLLF becomes

$$L=nN_f\ln\pi+(n-m)N_f\ln S_e+\sum_{k=1}^{N_f}\ln|\mathbf{H}_k|+\sum_{k=1}^{N_f}\ln|\mathbf{P}_k|+S_e^{-1}(d-\sum_{k=1}^{N_f}\mathbf{r}_k^*\mathbf{P}_k^{-1}\mathbf{r}_k) \tag{A.17}$$

where $d=\sum_{k=1}^{N_f}\hat{\mathbf{F}}_k^*\hat{\mathbf{F}}_k,\mathbf{r}_k=\bar{\mathbf{\Phi}}^T\hat{\mathbf{F}}_k$. Notice that $\mathbf{H}_k$ and $\mathbf{P}_k$ are related to all parameters, while $\mathbf{r}_k$ only depends on mode shapes.

Under the Gaussian approximation of the posterior PDF, the posterior covariance matrix is equal to the inverse of the Hessian of the NLLF. To simplify notations, we use a parenthesized variable in the superscript to denote differentiation with respect to that variable, that is, $L^{(x)}:=\frac{\partial L}{\partial x},L^{(x,y)}:=\frac{\partial^2 L}{\partial x\partial y}$. In doing so, the covariance $\hat{\mathbf{C}}$ of the corresponding parameters is

$$\hat{\mathbf{C}}=\left(L^{(\boldsymbol{\theta},\boldsymbol{\theta})}|_{\boldsymbol{\theta}=\hat{\boldsymbol{\theta}}}\right)^{-1} \tag{A.18}$$

and the 2nd order derivatives $L^{(\theta_i,\theta_j)},\forall\theta_i,\theta_j\in\boldsymbol{\theta}=(\mathbf{f},\zeta,\mathbf{\Phi},\mathbf{S},S_e)$ should be calculated, as are elaborated in the following.

To do so, we can divide the NLLF (A.17) into four parts,

$$L=L_e+L_H+L_P+L_q \tag{A.19}$$

where

$$\begin{aligned}
&L_e=nN_f\ln\pi+(n-m)N_f\ln S_e \quad , \quad L_H=\sum_{k=1}^{N_f}\ln|\mathbf{H}_k| \quad , \quad L_P=\sum_{k=1}^{N_f}\ln|\mathbf{P}_k|\\
&L_q=S_e^{-1}(d-q) \quad , \quad q=\sum_{k=1}^{N_f}\mathbf{r}_k^*\mathbf{P}_k^{-1}\mathbf{r}_k
\end{aligned} \tag{A.20}$$

so that $L^{(\theta_i,\theta_j)}=L_e^{(\theta_i,\theta_j)}+L_H^{(\theta_i,\theta_j)}+L_P^{(\theta_i,\theta_j)}+L_q^{(\theta_i,\theta_j)}$. Then, the derivatives are derived accordingly for the four parts:

- **Derivatives of L_e.**

  Notice that L_e depends only on S_e, and its Hessian matrix can be determined as

$$L_e^{(S_e,S_e)} = -(n-m)N_f S_e^{-2} \tag{A.21}$$

- **Derivatives of L_H.**

  L_H can be further separated into two parts,

$$\begin{aligned} L_H &= L_h + L_S; \\ L_h &= 2\sum_{k=1}^{N_f}\sum_{i=1}^{m} \ln|h_{ik}|, \quad L_S = N_f \ln|\mathbf{S}| \end{aligned} \tag{A.22}$$

  where L_h depends only on f_i, ζ_i and L_S depends only on $\mathbf{S}$. Thus, for all $x, y \in \{\mathbf{f}, \zeta\}$,

$$L_H^{(x,y)} = L_h^{(x,y)} = 2\sum_{k=1}^{N} \mathrm{Re}[h_{ik}^{-1}(h_{ik}^{(x,y)} - h_{ik}^{-1}h_{ik}^{(x)}h_{ik}^{(y)})], \tag{A.23}$$

$$h_{ik}^{(x,y)} = \begin{cases} 2\mathbf{i}(3\beta^2 + 1 + 2\mathbf{i}\zeta\beta)h_{ik}^3 f_k^{-2}, & \text{if } (x,y) = (f_i, f_i) \\ -8\zeta^2 h_{ik}^3, & \text{if } (x,y) = (\zeta_i, \zeta_i) \\ 2\mathbf{i}(3\beta^2 + 1 - 4\zeta^2 + 6\mathbf{i}\zeta\beta)h_{ik}^3, & \text{if } (x,y) = (f_i, \zeta_i) \text{ or } (x,y) = (\zeta_i, f_i) \\ 0, & \text{otherwise} \end{cases} \tag{A.24}$$

  and

$$h_{ik}^{(x)} = \begin{cases} -2(\beta + \mathbf{i}\zeta)h_{ik}^2, & \text{if } x = f_i \\ -2\mathbf{i}\beta h_{ik}^2, & \text{if } x = \zeta_i \\ 0, & \text{otherwise} \end{cases} \tag{A.25}$$

  where $\beta = f_i/f_k$. While for derivatives with respect to $\mathbf{S}$, there is

$$L_H^{(S_{ij},S_{rs})} = L_S^{(S_{ij},S_{rs})} = -2N_f(1+\delta_{ij})^{-1}(1+\delta_{rs})^{-1}\mathrm{Re}[S_{si}^{-1}S_{jr}^{-1} + S_{ri}^{-1}S_{js}^{-1}] \tag{A.26}$$

  where S_{ij} denotes the (i,j)-entry of $\mathbf{S}$.

- **Derivatives of L_P.**

  Notice that the derivatives of L_P are

$$L_P^{(x,y)} = \sum_{k=1}^{N_f} \mathrm{tr}[\mathbf{P}_k^{-1}(\mathbf{P}_k^{(x,y)} - \mathbf{P}_k^{(x)}\mathbf{P}_k^{-1}\mathbf{P}_k^{(y)})], \tag{A.27}$$

  where the first-order derivatives are of the form

$$\mathbf{P}_k^{(x)} = \begin{cases} -S_e\mathbf{H}_k^{-1}\mathbf{H}_k^{(x)}\mathbf{H}_k^{-1}, & \text{if } x \in \{\mathbf{f}, \zeta, \mathbf{S}\} \\ \mathbf{H}_k^{-1}, & \text{if } x = S_e \\ \bar{\mathbf{\Phi}}^{(\Phi_{ij})T}\bar{\mathbf{\Phi}} + \bar{\mathbf{\Phi}}^T\bar{\mathbf{\Phi}}^{(\Phi_{ij})}, & \text{if } x = \Phi_{ij} \end{cases} \tag{A.28}$$

  and the second-order derivatives are

$$\mathbf{P}_k^{(x,y)} = \begin{cases} -S_e\mathbf{H}_k^{-1}[\mathbf{H}_k^{(x,y)} - \mathbf{H}_k^{(y)}\mathbf{H}_k^{-1}\mathbf{H}_k^{(x)} - \mathbf{H}_k^{(x)}\mathbf{H}_k^{-1}\mathbf{H}_k^{(y)}]\mathbf{H}_k^{-1}, & \text{if } x,y \in \{\mathbf{f}, \zeta, \mathbf{S}\} \\ -\mathbf{H}_k^{-1}\mathbf{H}_k^{(x)}\mathbf{H}_k^{-1}, & \text{if } x \in \{\mathbf{f}, \zeta, \mathbf{S}\}, y = S_e \\ 2\,\mathrm{Sym}(\bar{\mathbf{\Phi}}^{(\Phi_{ij},\Phi_{rs})T}\bar{\mathbf{\Phi}} + \bar{\mathbf{\Phi}}^{(\Phi_{ij})T}\bar{\mathbf{\Phi}}^{(\Phi_{rs})}), & \text{if } (x,y) = (\Phi_{ij}, \Phi_{rs}) \\ \mathbf{0}, & \text{otherwise} \end{cases} \tag{A.29}$$

with $\mathrm{Sym}(\mathbf{A}) = (\mathbf{A} + \mathbf{A}^T)/2$ denoting the symmetric part of the real matrix $\mathbf{A}$. In the above equations, the derivatives of $\mathbf{H}_k$ and $\bar{\mathbf{\Phi}}$ should also be clarified, as presented in the following,

$$\mathbf{H}_k^{(x)} = \begin{cases} h_{ik}^{(x)*}\mathbf{h}_k\mathbf{S}\mathbf{e}_{ii} + h_{ik}^{(x)}\mathbf{e}_{ii}\mathbf{S}\mathbf{h}_k^*, & \text{if } x = f_i \text{ or } \zeta_i \\ h_{ik}h_{ik}^*\mathbf{e}_{ii}, & \text{if } x = S_{ii} \end{cases} \tag{A.30}$$

$$\mathbf{H}_k^{(x,y)} = \begin{cases} 2\,\mathrm{Her}[S_{ij}h_{ik}^{(x)}h_{jk}^{(y)*}\mathbf{e}_{ij} + \delta_{ij}h_{ik}^{(x,y)*}\mathbf{h}_k\mathbf{S}\mathbf{e}_{ii}], & \text{if } x = f_i \text{ or } \zeta_i, y = f_j \text{ or } \zeta_j \\ 0, & \text{otherwise} \end{cases} \tag{A.31}$$

where $\mathbf{e}_{ij}$ is a $m \times m$ matrix with the (i,j)-entry equaling to 1 and others being 0, $\mathrm{Her}(\mathbf{A}) = (\mathbf{A} + \mathbf{A}^*)/2$ represents the Hermitian part of the complex matrix $\mathbf{A}$. By definition $\bar{\mathbf{\Phi}} = [\phi_1/||\phi_1||, \phi_2/||\phi_2||, \ldots, \phi_m/||\phi_m||]$ and thus

$$\bar{\mathbf{\Phi}}^{(\Phi_{ij})} = ||\phi_j||^{-1}[\mathbf{e}_i - \bar{\Phi}_{ij}\bar{\mathbf{\Phi}}(j)]\mathbf{e}_j^T \tag{A.32}$$

$$\bar{\mathbf{\Phi}}^{(\Phi_{ij},\Phi_{rs})} = ||\phi_j||^{-2}[(3\bar{\Phi}_{ij}\bar{\Phi}_{rj} - \delta_{ir})\bar{\mathbf{\Phi}}(j) - \bar{\Phi}_{ij}\mathbf{e}_r - \bar{\Phi}_{rj}\mathbf{e}_i]\mathbf{e}_j^T\delta_{js} \tag{A.33}$$

where $\mathbf{e}_i$ is an n-by-1 vector with the ith entry equal to 1 and all other entries equal to zero, $\bar{\Phi}_{ij}$ denotes the (i,j)-entry of $\bar{\mathbf{\Phi}}$ and $\bar{\mathbf{\Phi}}(j)$ the jth column of $\bar{\mathbf{\Phi}}$.

- **Derivatives of L_q.**

  It is deduced that

$$L_q^{(x,y)} = \begin{cases} -S_e^{-1}q^{(x,y)}, & \text{if } x, y \in \{\mathbf{f}, \zeta, \mathbf{S}, \mathbf{\Phi}\} \\ S_e^{-2}[L_q - q^{(S_e)}] - S_e^{-1}[L_q^{(S_e)} - q^{(S_e,S_e)}], & \text{if } (x,y) = (S_e, S_e) \\ S_e^{-2}q^{(x)} - S_e^{-1}q^{(x,S_e)}, & \text{if } x \in \{\mathbf{f}, \zeta, \mathbf{S}, \mathbf{\Phi}\}, y = S_e \end{cases} \tag{A.34}$$

  where the first-order derivatives of L_q are

$$L_q^{(x)} = \begin{cases} -S_e^{-1}[L_q - q^{(S_e)}], & \text{if } x = S_e, \\ -S_e^{-1}q^{(x)}, & \text{if } x \in \{\mathbf{f}, \zeta, \mathbf{S}, \mathbf{\Phi}\}. \end{cases} \tag{A.35}$$

  To accomplish the above calculations, the first-order derivatives of q are given by

$$q^{(x)} = \begin{cases} \sum_{k=1}^{N_f}\mathbf{r}_k^*(\mathbf{P}_k^{-1})^{(x)}\mathbf{r}_k, & \text{if } x \in \{\mathbf{f}, \zeta, \mathbf{S}, S_e\} \\ \sum_{k=1}^{N_f}\mathbf{r}_k^*(\mathbf{P}_k^{-1})^{(\Phi_{rs})}\mathbf{r}_k + 2\mathrm{Re}\sum_k \hat{\mathbf{F}}_k(r)\mathbf{r}_k^*\mathbf{P}_k^{-1}(s), & \text{if } x = \Phi_{rs} \end{cases} \tag{A.36}$$

  where $\hat{\mathbf{F}}_k(r)$ denotes the rth entry of $\hat{\mathbf{F}}_k$ and $\mathbf{P}_k^{-1}(s)$ denotes the sth column of $\mathbf{P}_k^{-1}$. The second-order derivatives of q are

$$q^{(x,y)} = \begin{cases} \sum_k \mathbf{r}_k^*(\mathbf{P}_k^{-1})^{(x,y)}\mathbf{r}_k, & \text{if } x, y \in \{\mathbf{f}, \zeta, \mathbf{S}, S_e\} \\ \sum_k \mathbf{r}_k^*(\mathbf{P}_k^{-1})^{(x,\Phi_{ij})}\mathbf{r}_k + 2\mathrm{Re}\sum_{k=1}^{N_f}\hat{\mathbf{F}}_k^*\mathbf{r}_k^*(\mathbf{P}_k^{-1})^{(x)}, & \text{if } x \in \{\mathbf{f}, \zeta, \mathbf{S}, S_e\}, y = \Phi_{ij} \\ \sum_k \mathbf{r}_k^*(\mathbf{P}_k^{-1})^{(\Phi_{ij},\Phi_{rs})}\mathbf{r}_k + 2\mathrm{Re}\sum_k \mathbf{r}_k^*(\mathbf{P}_k^{-1})^{(\Phi_{ij})}\mathbf{r}_k^{(\Phi_{rs})} + & \\ 2\mathrm{Re}\sum_k \mathbf{r}_k^*(\mathbf{P}_k^{-1})^{(\Phi_{rs})}\mathbf{r}_k^{(\Phi_{ij})} + 2\mathrm{Re}\sum_k \mathbf{r}_k^{*(\Phi_{rs})}\mathbf{P}_k^{-1}\mathbf{r}_k^{(\Phi_{ij})} & \\ +2\mathrm{Re}\sum_k \mathbf{r}_k^*\mathbf{P}_k^{-1}\mathbf{r}_k^{(\Phi_{ij},\Phi_{rs})}, & \text{if } x = \Phi_{ij}, y = \Phi_{rs} \end{cases} \tag{A.37}$$

  with

$$\mathbf{r}_k^{(\Phi_{ij})} = \bar{\mathbf{\Phi}}^{(\Phi_{ij})T}\hat{\mathbf{F}}_k, \tag{A.38}$$

$$\mathbf{r}_k^{(\Phi_{ij},\Phi_{rs})} = \bar{\mathbf{\Phi}}^{(\Phi_{ij},\Phi_{rs})T}\hat{\mathbf{F}}_k. \tag{A.39}$$

  Herein, the involved derivatives $\bar{\mathbf{\Phi}}^{(\Phi_{ij})}, \bar{\mathbf{\Phi}}^{(\Phi_{ij},\Phi_{rs})}$ are readily presented in Eqs. (A.32) and (A.33), while the derivatives $(\mathbf{P}_k^{-1})^{(x)} = -\mathbf{P}_k^{-1}\mathbf{P}_k^{(x)}\mathbf{P}_k^{-1}, (\mathbf{P}_k^{-1})^{(x,y)} = -\mathbf{P}_k^{-1}[\mathbf{P}_k^{(x,y)} - \mathbf{P}_k^{(y)}\mathbf{P}_k^{-1}\mathbf{P}_k^{(x)} - \mathbf{P}_k^{(x)}\mathbf{P}_k^{-1}\mathbf{P}_k^{(y)}]\mathbf{P}_k^{-1}$ are computed by referring to Eqs. (A.28) and (A.29).

References

[1] E. Reynders. System identification methods for operational modal analysis: review and comparison. Arch. Comput. Methods Eng. 19 (2012), pp. 51–124. https://doi.org/10.1007/s11831-012-9069-x.

[2] R. Brincker and C. Ventura. Introduction to Operational Modal Analysis. Chichester, UK: Wiley, 2015. https://doi.org/10.1002/9781118535141.

[3] B. Peeters and G. De Roeck. Stochastic system identification for operational modal analysis: a review. J. Dyn. Syst. Meas. Control 123.4 (2001), pp. 659–667. https://doi.org/10.1115/1.1410370.

[4] C. Rainieri and G. Fabbrocino. Operational Modal Analysis of Civil Engineering Structures. New York: Springer, 2014. https://doi.org/10.1007/978-1-4939-0767-0.

[5] L. Zhang and R. Brincker. An overview of operational modal analysis: major development and issues. Proceedings of the 1st International Operational Modal Analysis Conference. Aalborg Universitet. Copenhagen, Denmark, 2005, pp. 179–190.

[6] P. Avitabile. Experimental modal analysis. Sound Vib. 35.1 (2001), pp. 20–31. https://doi.org/10.1002/9781119222989.

[7] B. Schwarz and M. Richardson. Experimental modal analysis. Proceedings of the CSI Reliability Week. Orlando, Florida, 1999.

[8] C. Devriendt et al. Structural health monitoring of offshore wind turbines using automated operational modal analysis. Struct. Health Monit. 13.6 (2014), pp. 644–659. https://doi.org/10.1177/1475921714556568.

[9] N.-J. Jacobsen, P. Andersen, and R. Brincker. Using enhanced frequency domain decomposition as a robust technique to harmonic excitation in operational modal analysis. Proceedings of ISMA2006: international conference on noise & vibration engineering. Katholieke Universiteit. 2006.

[10] J. S. Bendat and A. G. Piersol. Engineering Applications of Correlation and Spectral Analysis. New York: Wiley, 1980.

[11] H. A. Cole Jr. On-line failure detection and damping measurement of aerospace structures by random decrement signatures. Tech. rep. NASA, 1973.

[12] R. Brincker, L. Zhang, and P. Andersen. Modal identification of output-only systems using frequency domain decomposition. Smart Mater. Struct. 10.3 (2001), pp. 441–445. https://doi.org/10.1088/0964-1726/10/3/303.

[13] B. Peeters and G. De Roeck. Reference-based stochastic subspace identification for output-only modal analysis. Mech. Syst. Signal Process. 13.6 (1999), pp. 855–878. https://doi.org/10.1006/mssp.1999.1249.

[14] A. Belouchrani et al. A blind source separation technique using second-order statistics. IEEE Trans. Signal Process. 45.2 (1997), pp. 434–444. https://doi.org/10.1109/78.554307.

[15] P. Guillaume et al. A poly-reference implementation of the least-squares complex frequency-domain estimator. Proceedings of IMAC. USA, 2003.

[16] E. Reynders et al. Uncertainty quantification in operational modal analysis with stochastic subspace identification: Validation and applications. Mech. Syst. Signal Process. 66 (2016), pp. 13–30. https://doi.org/10.1016/j.ymssp.2015.04.018.

[17] D. Liu et al. Machine-learning-based methods for output-only structural modal identification. Struct. Control Health Monit. 28 (2021), e2843. https://doi.org/10.1002/stc.2843.

[18] C. Fevotte and S. J. Godsill. A Bayesian approach for blind separation of sparse sources. IEEE Trans. Audio Speech Lang. Process. 14.6 (2006), pp. 2174–2188. https://doi.org/10.1109/TSA.2005.858523.

[19] S. Wu et al. Hierarchical stochastic model in Bayesian inference for engineering applications: Theoretical implications and efficient approximation. ASCE-ASME J. Risk Uncertain. Eng. Syst. Part B Mech. Eng. 5.1 (2019), p. 011006. https://doi.org/10.1115/1.4040571.

[20] P. Angelikopoulos, C. Papadimitriou, and P. Koumoutsakos. Bayesian uncertainty quantification and propagation in molecular dynamics simulations: a high performance computing framework. J. Chem. Phys. 137.14 (2012). https://doi.org/10.1063/1.4757266.

[21] J. L. Beck. Bayesian system identification based on probability logic. Struct. Control Health Monit. 17.7 (2010), pp. 825–847. https://doi.org/10.1002/stc.424.

[22] K.-V. Yuen and L. S. Katafygiotis. Bayesian time–domain approach for modal updating using ambient data. Probabilist. Eng. Mech. 16.3 (2001), pp. 219–231. https://doi.org/10.1016/S0266-8920(01)00004-2.

[23] K.-V. Yuen and L. S. Katafygiotis. Bayesian fast Fourier transform approach for modal updating using ambient data. Adv. Struct. Eng. 6.2 (2003), pp. 81–95. https://doi.org/10.1260/136943303769013183.

[24] S.-K. Au. Fast Bayesian FFT method for ambient modal identification with separated modes. J. Eng. Mech. 137.3 (2011), pp. 214–226. https://doi.org/10.1061/(ASCE)EM.1943-7889.0000213.

[25] S. Au. Uncertainty law in ambient modal identification—part I: Theory. Mech. Syst. Signal Process. 48.1–2 (2014), pp. 15–33. https://doi.org/10.1016/j.ymssp.2013.07.016.

[26] S. Au, F.-L. Zhang, and Y. Ni. Bayesian operational modal analysis: theory, computation, practice. Comput. Struct. 126 (2013), pp. 3–14. https://doi.org/10.1016/j.compstruc.2012.12.015.

[27] Z. Zhu et al. Bayesian operational modal analysis with multiple setups and multiple (possibly close) modes. Mech. Syst. Signal Process. 150 (2021), p. 107261. https://doi.org/10.1016/j.ymssp.2020.107261.

[28] S.-K. Au. Fast Bayesian ambient modal identification in the frequency domain, part I: Posterior most probable value. Mech. Syst. Signal Process. 26 (2012), pp. 60–75. https://doi.org/10.1016/j.ymssp.2011.06.017.

[29] S.-K. Au. Operational Modal Analysis. Singapore: Springer, 2017. https://doi.org/10.1007/978-981-10-4118-1.

[30] B. Li and S.-K. Au. An expectation-maximization algorithm for Bayesian operational modal analysis with multiple (possibly close) modes. Mech. Syst. Signal Process. 132 (2019), pp. 490–511. https://doi.org/10.1016/j.ymssp.2019.06.036.

[31] C. Liu, D. Rubin, and Y. Wu. Parameter expansion to accelerate EM: the PX-EM algorithm. Biometrika 85.4 (1998), pp. 755–770. https://doi.org/10.1093/biomet/85.4.755.

[32] Z. Zhu, S.-K. Au, and B. Li. Accelerating convergence in Bayesian operational modal analysis with Fisher information matrix. Mech. Syst. Signal Process. 186 (2023), p. 109894. https://doi.org/10.1016/j.ymssp.2022.109894.

[33] W. Zhu, B. Li, and B. Spencer. From Expectation-Maximization to Newton: A more efficient implementation of Bayesian FFT method for operational modal analysis. SSRN Electron. J. (2024). Preprint. Available at: https://ssrn.com/abstract=4699147.

[34] C.-X. Qu et al. Closely spaced modes identification through modified frequency domain decomposition. Measurement 128 (2018), pp. 388–392. https://doi.org/10.1016/j.measurement.2018.07.006.

[35] L. Wang, M. Huang, and Z.-R. Lu. Blind separation of structural modes by compact-bandwidth regularization. Mech. Syst. Signal Process. 131 (2019), pp. 288–316. https://doi.org/10.1016/j.ymssp.2019.05.051.

[36] R. Castiglione, J. Antoni, and L. Garibaldi. Separation and identification of structural modes in largely underdetermined scenarios using frequency banding. J. Sound Vib. 414 (2018), pp. 192–217. https://doi.org/10.1016/j.jsv.2017.10.033.

[37] J. Antoni and S. Chauhan. Study and extension of second-order blind source separation to operational modal analysis. J. Sound Vib. 332 (2013), pp. 1079–1106. https://doi.org/10.1016/j.jsv.2012.09.016.

[38] W. Zhou and D. Chelidze. Blind source separation based vibration mode identification. Mech. Syst. Signal Process. 21.8 (2007), pp. 3072–3087. https://doi.org/10.1016/j.ymssp.2007.05.007.

[39] D. Ehrhardt et al. Veering and nonlinear interactions of a clamped beam in bending and torsion. J. Sound Vib. 416 (2018), pp. 1–16. https://doi.org/10.1016/j.jsv.2017.11.045.

[40] Y. Ni et al. Technology innovation in developing the structural health monitoring system for Guangzhou New TV Tower. Struct. Control Health Monit. 16.1 (2009), pp. 73–98. https://doi.org/10.1002/stc.291.

[41] W. Chen et al. Theoretical and experimental modal analysis of the Guangzhou New TV Tower. Eng. Struct. 33.12 (2011), pp. 3628–3646. https://doi.org/10.1016/j.engstruct.2011.07.028..

[42] S. Kuok and K. Yuen. Structural health monitoring of Canton Tower using Bayesian framework. Smart Struct. Syst. 10.4–5 (2012), pp. 375–391. https://doi.org/10.12989/sss.2012.10.4_5.375.

[43] F. Zhang et al. Operational modal analysis of Canton Tower by a fast frequency domain Bayesian method. Smart Struct. Syst. 17.2 (2016), pp. 209–230. https://doi.org/10.12989/sss.2016.17.2.209.

[44] Y. Ni et al. SHM benchmark for high-rise structures: A reduced-order finite element model and field measurement data. Smart Struct. Syst. 10.4 (2012), pp. 411–426. https://doi.org/10.12989/sss.2012.10.4_5.411.